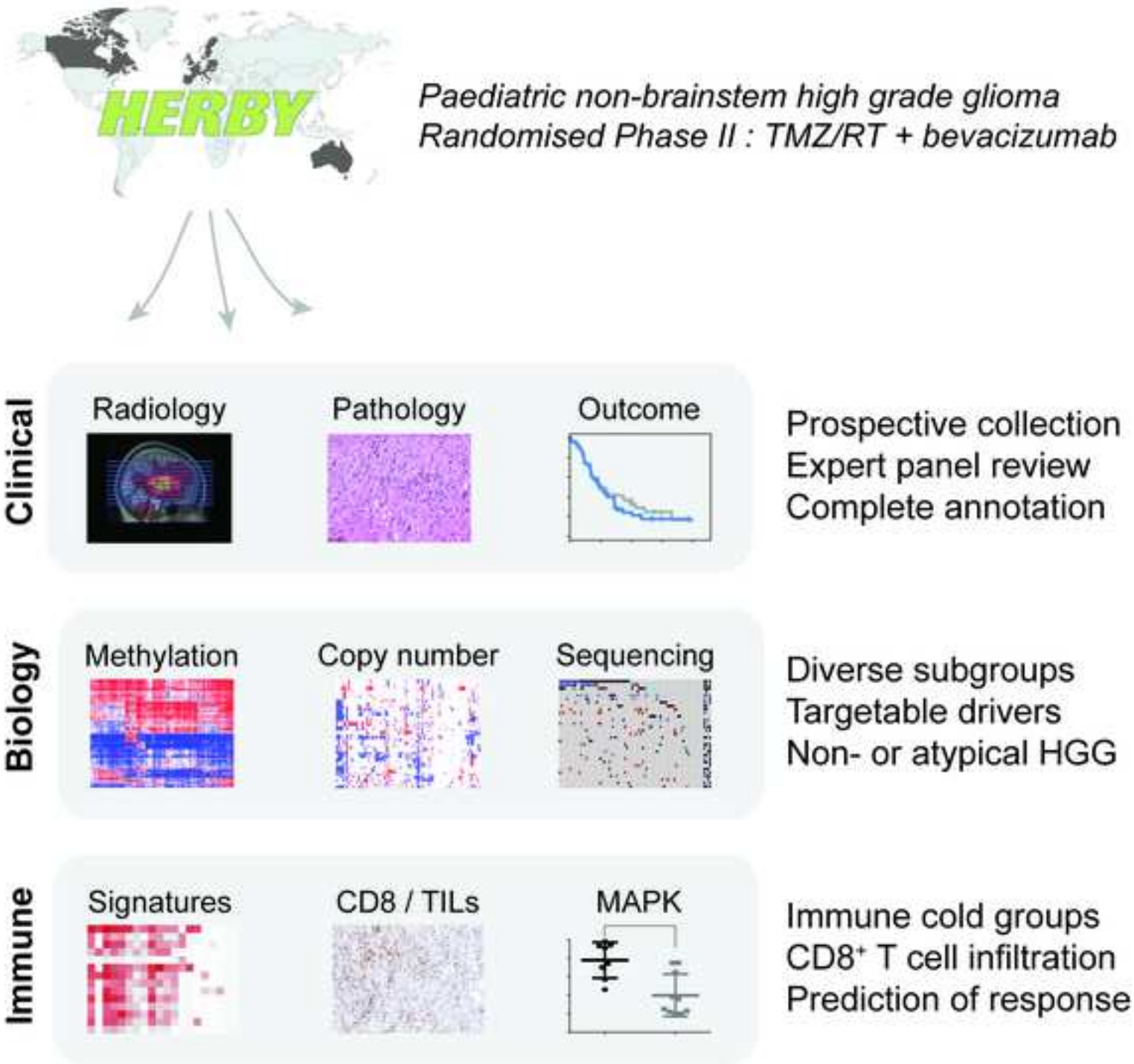

Molecular, pathological, radiological and immune profiling of non-brainstem paediatric high grade glioma from the HERBY phase II randomised trial

Alan Mackay[1,2], Anna Burford[1,2], Valeria Molinari[1,2], David TW Jones[3,4], Elisa Izquierdo[1,2], Jurriaan Brouwer-Visser[5], Felice Giangaspero[6,7], Christine Haberler[8], Torsten Pietsch[9], Thomas S Jacques[10,11], Dominique Figarella-Branger[12], Daniel Rodriguez[13], Paul S Morgan[13], Pichai Raman[14,15], Angela J. Waanders[14,16], Adam Resnick[14,15,16], Maura Massimino[17], Maria Luisa Garre[18], Helen Smith[19], David Capper[20,21], Stefan M Pfister[3,4], Thomas Würdinger[22], Rachel Tam[23], Josep Garcia[19], Meghna Das Thakur[23], Gilles Vassal[24], Jacques Grill[24], Tim Jaspan[13], Pascale Varlet[25] and Chris Jones[1,2]

Divisions of [1]Molecular Pathology and [2]Cancer Therapeutics The Institute of Cancer Research, London, UK; [3]Division of Paediatric Neuro-oncology, German Cancer Consortium (DKTK), German Cancer Research Centre (DKFZ), Heidelberg, Germany; [4]Hopp Children's Cancer Center at the NCT Heidelberg (KiTZ), Heidelberg, Germany [5]Roche Innovation Center, New York, NY, USA; [6]Department of Radiology, Oncology and Anatomic-Pathology Sciences, Sapienza University, Rome, Italy; [7]IRCCS Neuromed, Pozzilli, Italy; [8]Institute of Neurology, Comprehensive Cancer Center, Medical University of Vienna, Vienna, Austria; [9]DGNN Brain Tumor Reference Center, Institute of Neuropathology, University of Bonn Medical Center, Bonn, Germany; [10]UCL Great Ormond Street Institute of Child Health, London, UK; [11]Department of Histopathology, Great Ormond Street Hospital for Children, London, UK; [12]Department of Pathology and Neuropathology, La Timone Hospital, Aix Marseille University, Marseille, France; [13]Nottingham University Hospitals, Nottingham, UK; [14]The Center for Data Driven Discovery in Biomedicine (D[3]b) and Divisions of Neurosurgery[15] and Oncology[16], Children's Hospital of Philadelphia, Philadelphia PA, USA; [17]Pediatric Oncology Unit, Fondazione IRCCS, Istituto Nazionale Tumori, Milan, Italy; [18]Centro di Neuro-Oncologia, Istituto Giannina Gaslini, Genoa, Italy; [19]F. Hoffmann-La Roche Ltd, Basel, Switzerland; [20]Charité – Universitätsmedizin Berlin, corporate member of Freie Universität Berlin, Humboldt-Universität zu Berlin, Germany; [21]Berlin Institute of Health, Institute of Neuropathology, Germany; [22]VU Medical Center, Amsterdam, Netherlands; [23]Genentech, South San Francisco, CA, USA; [24]Pediatric and Adolescent Oncology and Unite Mixte de Recherche 8203 du Centre National de la Recherche Scientifique, Gustave Roussy, Paris-Saclay University, Villejuif, France; [25]Sainte-Anne Hospital, Paris-Descartes University, Paris, France

***Lead contact, and correspondence to*:**

Chris Jones, Centre for Evolution and Cancer, Divisions of Molecular Pathology and Cancer Therapeutics, The Institute of Cancer Research, 15 Cotswold Road, Sutton, Surrey, SM2 5NG, UK, chris.jones@icr.ac.uk, +44 (0)20 8722 4416

Key words: immune, CD8, MAPK, hypermutator, H3F3A, paediatric high grade glioma,

Running title: Molecular profiling of pHGG from HERBY

Summary

The HERBY trial was a phase-II open-label, randomised, multicentre trial evaluating bevacizumab (BEV) in addition to temozolomide/radiotherapy in patients with newly-diagnosed non-brainstem high-grade glioma (HGG) between the ages of 3-18 years. We carried out comprehensive molecular analysis integrated with pathology, radiology and immune profiling. In post-hoc subgroup analysis, hypermutator tumours (mismatch repair deficiency and somatic *POLE*/*POLD1* mutations) and those biologically resembling pleomorphic xanthoastrocytoma (PXA-like, driven by BRAF_V600E or *NF1* mutation) had significantly more $CD8^+$ tumour-infiltrating lymphocytes, and longer survival with the addition of BEV. Histone H3 subgroups (hemispheric G34R/V and midline K27M) had a worse outcome and were immune cold. Future clinical trials will need to take into account the diversity represented by the term 'HGG' in the paediatric population.

Significance

We validate in the prospective clinical trial setting the biological and clinical diversity of paediatric high grade glioma previously described in large retrospective series, underpinned by detailed pathological and radiological analysis. Although adding bevacizumab (BEV) to standard temozolomide/radiotherapy did not improve survival across the whole cohort, we identify disease subgroups with MAPK activation to harbour an enhanced $CD8^+$ T cell immune response, which may derive benefit from the addition of BEV. If confirmed in another study, this would represent the first predictive biomarker for this regimen in these tumours, and points the way for new therapeutic strategies for subgroups of children with high grade glioma.

Introduction

High grade gliomas (HGG) in children, like their adult counterparts, continue to have a bleak prognosis, with a median overall survival of 9-15 months (Cohen et al., 2011; Jones et al., 2016; Ostrom et al., 2015). Recent integrated molecular profiling initiatives have shown that paediatric HGG are biologically distinct from their adult counterparts, with subgroups of the disease marked by recurrent mutations in genes encoding histone H3 variants having different age of incidence, anatomical location, clinical outcome, and a range of biological parameters (Jones and Baker, 2014; Mackay et al., 2017; Paugh et al., 2010; Schwartzentruber et al., 2012; Sturm et al., 2012; Wu et al., 2012; Wu et al., 2014). Histone wild-type tumours have widely differing mutational burdens, ranging from infant cases (<3 years) driven by single gene fusion events through to patients with biallelic mismatch repair deficiency harbouring some of the highest mutational rates in human cancer (Jones and Baker, 2014; Mackay et al., 2017; Shlien et al., 2015; Wu et al., 2014).

The rapid advances in our understanding of paediatric HGG have come predominantly from the accumulation of numerous disparate retrospective collections, a reflection of the rarity of the disease. Clinical trial cohorts with ancillary biomarker analyses have been relatively limited in their scope, and historically have focussed on single marker analyses. These include the Children's Oncology Group ACNS0126 (radiotherapy (RT) / temozolomide (TMZ))(Cohen et al., 2011) and ACNS0423 (RT/TMZ followed by TMZ and lomustine)(Jakacki et al., 2016) studies, which report on the frequency and clinical correlations of MGMT expression (ACNS0126)(Jakacki et al., 2016; Pollack et al., 2006), *IDH1* mutation (ACNS0423)(Pollack et al., 2011) as well as phosphorylated Akt expression(Pollack et al., 2010a) and microsatellite instability (both)(Pollack et al., 2010b). The CCG-945 study ("8 in 1" chemotherapy)(Finlay et al., 1995) first reported on the prognostic significance of p53 expression/mutation (Pollack et al., 2002), in addition to the presence/absence of 1p19q co-deletion (Pollack et al., 2003b).

This latter study also highlighted the critical importance of pathological review in the diagnosis of paediatric HGG, and subsequent interpretation of clinical trial results (Gilles et al., 2008; Pollack et al., 2003a), particularly in midline locations (Eisenstat et al., 2015). It has subsequently become clear that numerous histological subtypes of HGG can harbour distinct genetic drivers and have considerably better clinical outcomes, such as *BRAF* V600E mutations in epithelioid glioblastoma (GBM), anaplastic ganglioglioma and anaplastic pleomorphic xanthoastrocytoma (PXA) (Hatae et al., 2016); in the latter two categories, this overlaps with the lower-grade entities lacking obvious anaplasia. Additional histone wild-type cases of otherwise uncontroversial HGG have been found to be biologically and clinically more similar to several types of low grade glioma (LGG) and PXA (Korshunov et al., 2015), highlighting the importance of an integrated diagnosis combining molecular and histological features.

The HERBY trial (study BO25041; clinicaltrials.gov NCT01390948) was a phase II, open-label, randomised, multicentre, comparator study of the addition of the anti-angiogenic agent bevacizumab (BEV) to radiotherapy (RT) and temozolomide (TMZ) in patients between the ages of 3-18 years with newly-diagnosed non-brainstem HGG (Grill et al., 2018). Central confirmation of HGG diagnosis was mandatory before randomisation, followed by consensus review by five independent expert neuropathologists. Real-time panel radiological assessment was also incorporated. An exploratory endpoint of the study was to establish a biospecimen repository for correlative molecular profiling. In addition to its role in tumour angiogenesis, VEGF restricts immune cell activity, and BEV has been demonstrated to facilitate recruitment of T cells to infiltrate tumours (Wallin et al., 2016), as well as increase the ratio of CD8/CD3-positive T cells in adult glioblastoma specimens (Scholz et al., 2016). We therefore also sought to explore the immune profile of cases within the HERBY cohort. Through an integrated analysis of biological, clinicopathological, radiological and immunological variables, we provide a detailed description of the diversity of the trial cohort, and identify disease subgroups with an elevated immune response who benefited from the addition of BEV.

Results

The translational research cohort is representative of the whole clinical trial population

The total HERBY cohort comprised 121 randomised patients at diagnosis (3-18 years) plus three infant cases (<3 years) at relapse. Of these, 113 patients consented to the translational research programme (Table S1A). Tumour tissue was collected either from resection (n=93) or biopsy (n=20), although 24 cases failed to provide either sufficient quantity or quality of sample for molecular analysis. For the remaining 89 cases, material was available in the form of either fresh frozen material (FF, n=36), formalin-fixed paraffin embedded pathology specimens (FFPE, n=79), or both (n=26). These were subjected to Sanger sequencing for H3F3A (n=89), exome sequencing (n=86), Illumina 450k methylation BeadArray profiling (n=74), CD8 immunohistochemistry (n=70), MS-PCR for MGMT promoter methylation (n=36), a capture-based sequencing panel for common fusion gene detection (n=68), and RNA sequencing (n=20) (Figure 1A).

The translational research cohort, representing a subset (91%) of the randomised trial, displayed equivalent clinical characteristics to the full dataset, with no difference in the primary end-point of 1 year event-free survival (EFS) with the addition of BEV to the standard therapy of temozolomide and radiotherapy (median 12.0 *versus* 8.3 months, p=0.605, log-rank test) (Figure 1) (Grill et al., 2018). The cohort contained 66 (58%) hemispheric and 47 (42%) non-brainstem midline tumours, with the latter location conferring a significantly shorter EFS (median 8.0 *versus* 14.7 months, p=0.00201, log-rank test) (Figure 1C). Histone mutation status was a significant predictor of worse prognosis for H3F3A_K27M (24/89, 27%; median EFS=7.9 months; p=0.0063, log-rank test) and also trended towards shorter survival for H3F3A_G34R/V (7/89, 8%; median EFS=8.3 months; p=0.096, log-rank test) (Figure 1D).

Integrated molecular analysis defines the major (epi)genomic alterations in pHGG

We used the Heidelberg brain tumour classifier on Illumina 450k methylation array data to assign a molecular subgroup to each of 74 samples for which such data was available (Table

S1B). After excluding low-scoring assignments (<0.2), we used a simplified system to classify tumours as either H3K27M (n=18), H3G34R/V (n=6) or IDH1 (n=4) (integrating gene mutation data in low-scoring cases); as resembling pleomorphic xanthoastrocytoma (PXA-like, n=9) or other low grade glioma (LGG-like, n=3); and aggregating the remaining tumours (HGG-WT, n=34) (Figure 2A). IDH1 tumours represented the oldest patients (median=17.2 years, others=11.2, p=0.0107, t-test), with LGG-like representing the youngest category (median=5.7 years, p=0.0098, t-test) (Figure 2B). These two subgroups each had significantly better outcome in terms of EFS (p=0.0281 and p=0.0386, log-rank test), though not overall survival (OS, p=0.0935 and p=0.129, log-rank test) (Figure 2C), when compared individually to the remaining tumours. The PXA-like showed a trend towards longer OS (p=0.0867, log-rank test) compared to the rest. When IDH1, PXA-like and LGG-like tumours were excluded from the analysis, the significant differences between histone mutant and HGG-WT groups were absent (H3K27M - p=0.257 EFS and p=0.0746 OS; H3G34R/V - p=0.552 EFS and p=0.116 OS, log-rank test). 12/78 (15%) samples harboured a methylated *MGMT* promoter, though this was largely restricted to the H3G34R/V (n=3, p=0.0249, Fishers exact test) and IDH1 (n=3, p=0.0062, Fishers exact test) subgroups (Figure 1A), and was not significantly associated with survival (Figure 1B) in these uniformly TMZ-treated patients.

We used 450k methylation array and exome sequencing coverage to derive DNA copy number profiles for 86 paediatric high grade glioma (pHGG) (Figure S1C). Taken with the somatic single nucleotide variants (SNVs) and small insertion/deletions (InDels) from whole exome sequencing (Table S1E), and candidate gene fusion events from capture-based panel sequencing (n=68) and RNAseq (n=20) (Table S1F), we derived an integrated map of genetic alterations across the translational research cohort (Figure 3A). The most common alteration was *TP53* mutation (39/82, 48%), followed by *ATRX* deletion/mutation (25/82, 30%), *PDGFRA* amplification/mutation (17/82, 21%) and *CDKN2A/B* deletion (15/82, 18%). Additional recurrent alterations in receptor tyrosine kinases (*EGFR, MET, ERBB3, IGF1R, NTRK2*), PI3-kinase/mTOR (*PTEN, PIK3CA, TSC2, PIK3R1*), and MAP-kinase (*NF1, BRAF, PTPN11,*

PTPN12) pathways were common, as were amplifications/mutations in various genes associated with cell cycle regulation (*RB1, CDK4, MDM2, CCND2*). Taking a minimum variant allele frequency of 5% as a threshold, the median number of somatic mutations per sample was 15 (range=0-337) (Figure 3B), with the exception of four cases for whom there were more than a hundred-fold more, and were excluded from gene-level counts.

Paediatric HGG comprise a diverse set of biological and clinicopathological subgroups

Two cases were highlighted from the methylation subgrouping as potentially representing non-HGG entities. One case classifying as CNS neuroblastoma with *FOXR2* activation (CNS NB-FOXR2, methylation classifier score=0.617), was found to have no evidence of FOXR2 alterations. A further case, a compact and necrotic tumour with perivascular radiating arrangements (Figure S2A), displayed a methylation classifier score strongly indicative of a high grade neuroepithelial tumour with *MN1* alteration (CNS HGNET-MN1, methylation classifier score=0.713) (Figure S2B). We identified a novel candidate alteration in this case fusing exon 1 of *MN1* (22q12.1) to exon 3 of *CARD6* (5p13.1) (Figure S2C), and thus appears most likely to fall into this categorization.

Three cases classified more closely to either pilocytic astrocytoma (PA, n=2) or desmoplastic infantile ganglioglioma (DIG, n=1) by 450k methylation profiling. The first two harboured MAPK dysregulation in the form of either *BRAF*_V600E or intragenic *FGFR1* duplication (Figure S2C). Histologically, after Pathology Committee re-review, no piloid features were seen, and anaplastic features were evident (Figure S2D). The DIG-like case was found in the infant cohort (2.7 years). None of these three patients died during the course of follow-up, and although numbers are small, were all found in the right frontal and temporo-parietal lobes with central predominance (Figure S2E).

There were four cases with *IDH1* hotspot mutations (Figure S3A). Three were classified as WHO grade III AA, IDH1_R132 positive by IHC, with concurrent *TP53* and *ATRX* mutations.

The remaining case was originally classified as a mixed oligo-astrocytoma, which by virtue of the presence of *IDH1*_R132 and *TERT* promoter mutation (C228T) as well as copy number loss of chromosomes 1p and 19q, would be described as an oligodendroglioma according to WHO 2016. (Figure S3B). Across the whole cohort, *IDH1* mutation conferred a significantly longer EFS (p=0.0398, log-rank test), though not OS (p=0.110, log-rank test) (Figure S3C), and were restricted to the frontal lobes (Figure S3D).

After excluding *IDH1* mutant cases, the remaining *H3F3A* and *BRAF* wild-type cases (n=38) represented a heterogeneous mix of genomic profiles, with recurrent deletions/mutations in the common pHGG tumour suppressor genes *TP53* (n=11), *ATRX* (n=5), *CDKN2A/B* (n=7), *NF1* (n=8), *RB1* (n=7) and *PTEN* (n=5), but also with an enrichment of gene amplifications in *PDGFRA* (n=5, with *KIT* and *KDR*, n=4), *CDK4* (n=7, with *MDM2*, n=4), *EGFR*, (n=4), *MET* (n=2), *CCND2* (n=3) and *MYCN* (n=3) (Figure S4A). The most common methylation subclass in these cases was designated 'GBM_RTK_MYCN' (n=6), however included only one of those with *MYCN* amplification, and with no other common amplifications or mutations. Seven cases harboured none of the recurrently altered genes previously described in pHGG, and clearly represent a subgroup which warrants further investigation. Together, these cases had bilateral hemispheric distribution with predominant deep right cerebral localization (Figure 4B).

H3F3A mutation confers poor prognosis for both K27M and G34R/V substitutions

Histone mutations have been shown to be present in approximately half of all pHGG (Mackay et al., 2017), with a clear negative impact on survival for K27M (Karremann et al., 2018; Khuong-Quang et al., 2012; Mackay et al., 2017), though the situation is less clear for G34R/V mutations (Bjerke et al., 2013; Korshunov et al., 2015; Mackay et al., 2017). There were seven cases with H3F3A_G34 substitutions (six G34R and one G34V), with 6/7 (86%) cases additionally harbouring *TP53* and/or *ATRX* mutations (5/7, 71% both), whilst 5/7 (71%) also contained *PDGFRA* amplification and/or mutation (Figure 4A). There were no other recurrent mutations, although isolated instances of mutations in PI3K signalling (*PIK3CA, PTEN*) and

DNA repair (*ERCC1*) were observed. Histologically, there were four GBM, two anaplastic astrocytoma (AA) with multinucleated cells and one HGG, NOS. (Figure 4B). Tumours were Olig2 negative (7/7) with strong nuclear accumulation of p53 (6/7). H3F3A_G34R/V mutant tumours had a tendency to being diffusely infiltrative with predominant deep left temporoparietal involvement (Figure 4C). Across all tumours within this hemispheric subgroup, patients harbouring these mutations trended towards a shorter EFS (median=8.3 months; p=0.0572, log-rank test) and had a significantly shorter OS (median=12.0 months; p=0.00765, log-rank test) (Figure 4D), though this association was lost when IDH1, PXA-like and LGG-like tumours were excluded (p=0.440 EFS and p=0.139 OS, log-rank test) (Figure S5A).

By contrast, K27M substitutions were restricted to midline regions (n=24). 15/21 (71%) exome sequenced cases carried additional amplifications/mutations in the RTK-PI3K pathway across a range of genes (*PDGFRA, MET, IGF1R, FGFR1, PTEN, PIK3CA, PIK3R1*), with 5/6 of the remaining tumours harbouring *ATRX* mutation. (Figure 4E). There was strong immunoreactivity for H3K27M in 12/12 cases tested. (Figure 4F). Two patients had distinct, separate lesions in the thalamus and hypothalamus, whilst the remaining had central thalamic, midbrain or cerebellar localization (Figure 4C). Although conferring a worse prognosis across the whole cohort (above), within midline locations there was no association with either EFS (median=7.9 months; p=0.482, log-rank test) or OS (median=14.2 months; p=0.839, log-rank test) (Figure 4G), nor any prognostic value for WHO grade in K27M tumours (p=0.646 EFS and p=0.762 OS, log-rank test) (Figure S5B).

Immune-positive subgroups are associated with MAPK and benefit from the addition of BEV

Paediatric HGGs with a high mutational burden had previously been described to have an elevated neoantigen load, and a pronounced immune response (Bouffet et al., 2016). Four cases were classed as hypermutator, with a median somatic mutation count of 4848

(range=2197-5332; mutation rate 160-240 mutation/Mb) (Figure 5A, Table S1A). Mutation signature analysis showed predominantly C>T transitions and hotspot somatic *POLE* mutations in three cases, and a somatic *POLD1* mutation in the fourth (Figure 5B). They were all categorised as glioblastoma, and in one case, the presumed mismatch repair deficiency was demonstrated by clear loss of MLH1 expression by immunohistochemistry (Figure 5C). This specimen had a heterogeneous immune phenotype, with a relatively high percentage of $CD8^+$ cells in the central area, and in three or four thin perivascular cuffs (Figure 5D). These hypermutator cases had the highest percentage of $CD8^+$ cells ($p<0.0001$ t-test *versus* rest excluding PXA-like) (Figure 5E). Notably, PXA-like tumours were also significantly enriched for $CD8^+$ cells ($p<0.0001$ t-test *versus* rest excluding hypermutator). Of three HGG-WT cases with relatively high immune infiltrate, two had elevated somatic SNV counts (100-110 per case), whilst the third scored highly for the "GBM_LYMPH_HI" subgroup by methylation profiling. A formal histological assessment of tumour infiltrating lymphocytes (TILs) confirmed the highest scoring categories (lymphocytes scattered amongst tumour cells / in more than 50% of the tumour) to be almost exclusively present in hypermutator and PXA-like subgroups (Figure S6A), as were those cases formally classified as an inflamed immune phenotype (Figure S6B). Histone mutant tumours were notably immune cold as defined by a lack of CD8-immunoreactivity and an absence of TILs.

Nine cases classified by 450k methylation profiling as more similar to PXAs than high grade gliomas. 5/9 (55%) harboured BRAF_V600E mutations, with 3/5 (60%) also containing *CDKN2A/B* deletions and/or *TERT* amplification or promoter mutation (C250T) (Figure 6A). 3/4 of the remaining cases were instead found with somatic *NF1* mutation, often in concert with *TP53* (3/4) and/or *ATRX* mutation (2/4). Upon histological re-review according to WHO 2016 guidelines by the HERBY Pathology Committee, *BRAF*_V600E cases were all found to comprise the epithelioid variant of grade IV glioblastoma, whilst the *NF1* cases were all classified as the giant cell variant (Figure 6B). PXA-like tumours had a high degree of immune infiltrate, with cases exhibiting several perivascular cuffs of more than three layers of CD8+ T

cells, which were also scattered among tumour cells in more than 50% of the specimen (Figure 6C). They were found bilaterally restricted to temporo-parietal regions with a medial hemispheric predominance (Figure 6D).

Gene expression data from RNA sequencing were available for a subset of samples, in which a CD8 T effector / T cell signature was found to correlate with CD8-positivity by immunohistochemistry (r^2=0.49138, p=0.00523), with two hypermutator cases as outliers (Figure 7A). Although no PXA-like or BRAF_V600E mutant cases were included in this subset, these signatures were particularly evident in cases with predicted MAPK pathway-activating alterations in *NF1* (truncating frameshift/nonsense, disrupting translocation or predicted damaging missense), *NTRK2* (translocation or tandem duplication of kinase domains) and *FGFR1* (known activating hotspot mutation) (Figure 7B). GSEA showed multiple enrichments for gene sets associated with T cell signalling and the immune response (*e.g*. PID_CD8_TCR_ DOWNSTREAM_PATHWAY, enrichment score=0.594, nominal p=0.0020; KEGG_T_CELL_RECEPTOR_SIGNALING_PATHWAY, enrichment score=0.532, nominal p=0.0297) and inflammatory-related MAPK signalling (*e.g*. ST_JNK_MAPK_PATHWAY, enrichment score=0.466, nominal p=0.0332; REACTOME_GRB2_SOS_PROVIDES_ LINKAGE_TO_MAPK_SIGNALING_FOR_INTERGRINS, enrichment score=0.581, nominal p=0.0239) (Table S2), with mean T effector / T cell signature significantly higher than in cases without MAPK alterations (p=0.0039, t-test) (Figure 7C). This was validated in a restricted cohort of n=59 patients from our retrospective analysis designed to approximate the HERBY cohort (*i.e.* non-brainstem pHGG aged 3-18 years), in which we observed a significantly elevated T effector / T cell gene expression signature in MAPK-altered samples (p=0.0018, t-test) (Figure S6C,D), further evidenced by GSEA (*e.g.* PID_CD8_TCR_ DOWNSTREAM_PATHWAY, enrichment score=0.551, nominal p=0.0099; BIOCARTA_TCR_PATHWAY enrichment score=0.520, nominal p=0.0305) (Table S2).

We also explored other immune-related gene expression signatures in the RNAseq data, and noted a trend towards an elevated macrophage M2 response in MAPK-altered tumours (p=0.0810, t-test) (Figure S6E,F). We performed CD68 staining for a limited number of cases with a histologically defined immune response (n=11), and found a heterogeneously distributed tumor-associated macrophages (TAM) component, comprising either TAM-free tumoral areas, or rich TAM areas especially around necrotic foci or associated with perivascular lymphocytes (Figure S6G). BRAF_V600E cases had CD68+ TAM more diffusely intermingled with tumour cells (Figure S6G). Although the presence of macrophage infiltration has previously been reported in diffuse intrinsic pontine glioma (Caretti et al., 2014), we observed no association of the M2 gene expression signature with K27M midline tumours in our cohort (p=0.965).

With the primary efficacy analysis failing to demonstrate survival differences between the two arms, we explored whether the molecular profiling data could identify subsets of patients who may have benefited from the addition of BEV to the standard chemoradiotherapy. We performed a univariate Cox regression analysis on methylation-based molecular subgroup as well as individual gene-level alterations, and found none which had significant difference in outcome between investigational arms (Figure S7A), although *NF1*, *PDGFRA* and *TP53* were adverse prognostic markers across the whole cohort (Figure S7B-E). Notably however, whilst not predictive in the TMZ/RT arm (Figure 7D), the presence of high levels of $CD8^+$ T cells within the central tumour area conferred a significantly better overall survival in children receiving the addition of BEV (p=0.0404, log-rank test) (Figure 7E). Fitting a Cox interaction model (with proportional hazards confirmed by calculating Schoenfeld residuals, p=0.268), high CD8 levels trended towards predictivity of response to TMZ/RT+BEV, with hazard ratio of 0.360 (p=0.066). In keeping with the strong subgroup associations described, 17/18 cases with high levels of $CD8^+$ T cells are hemispheric (representing 38.6% cases in this location). Within hemispheric tumours only, there is a significant interaction between high CD8 and BEV (HR=0.251, p=0.024).

Discussion

The HERBY trial opened in October 2011, prior to the discovery of histone gene mutations in 2012 (Schwartzentruber et al., 2012), and the more extensive genome sequencing published in 2014 (Wu et al., 2014), and there were no molecular markers incorporated into trial design. The present correlative biology study demonstrates the extent of the heterogeneous population of tumours, with widely differing biological drivers and clinicopathological features, which were included in the cohort. An important example is the four adolescent patients with *IDH1* mutation, who had a significantly better clinical outcome, and may now be thought of as the lower age limit of an adult subgroup rather than 'paediatric' HGG. Such patients will likely be included in future *IDH1*-focussed trials across adult and paediatric oncology services in order to maximize the possibility of positive trial outcomes. Similarly, within the HERBY cohort were seven patients with *BRAF*_V600E mutations, who would now be candidates for upfront trials of targeted inhibitors such as vemurafenib (Bautista et al., 2014; Robinson et al., 2014), and four hypermutator patients, with somatic *POLE/POLD1* mutations and likely harbouring biallelic mismatch repair deficiency syndrome, who may benefit from immune checkpoint inhibitors such as nivolumab (Bouffet et al., 2016). In both instances, early clinical data shows remarkably promising results and there would be little justification in their continued inclusion in catch-all HGG trials.

Notably, both hypermutator cases and those biologically resembling PXAs, the latter of which harboured either *BRAF* or *NF1*-driven MAP-kinase alterations, were found to be the most immunogenic in terms of $CD8^+$ T cells / tumour infiltrating lymphocytes, including a significantly elevated CD8 effector T cell gene expression signature. This is important given reports in adult glioblastoma of an immunosuppressive phenotype associated with an elevated $CD8^+$ regulatory T cell immune infiltrate (Kmiecik et al., 2013). The MAPK-altered hypermutator and PXA-like paediatric cases in the present cohort were found to benefit from the addition of BEV to TMZ/RT in regards overall, though not event-free survival, the first and only such predictive biomarker identified in this patient population. The immunomodulatory effects of anti-

angiogenic therapies have been previously demonstrated in other cancer types (Elamin et al., 2015), with VEGF-A shown to play an important role in the induction of an immunosuppressive environment (Gabrilovich et al., 1996), through increasing PD-L1 and other inhibitory checkpoints involved in $CD8^+$ T cell exhaustion.

An important implication of these observations is the possibility of overcoming resistance to BRAF/MEK-targeting therapies by combining them with BEV and/or other immune therapies in these subgroups, as has been suggested in melanoma (Hu-Lieskovan et al., 2015). Such a strategy is however complicated by the diverse roles on T cell function played by MAPK signalling. Although involved in the regulation of T cell proliferation and survival (D'Souza et al., 2008), selective BRAF inhibitors have been shown to increase $CD8^+$ lymphocytes in human metastatic melanoma models (Wilmott et al., 2012). Crucially, although MEK inhibition has been demonstrated to block naïve $CD8^+$ T cell priming in a colon cancer model, the number of $CD8^+$ effector T cells within the tumour were increased, and could potentiate immune checkpoint therapy (Ebert et al., 2016). A limitation of the present study is the small numbers in this *post hoc* analysis, and the benefit that patients with these biological subgroups may derive from an immunomodulatory mechanism of BEV would need to be tested in the prospective setting. This is a challenge given that these patients represent approximately 10-15% of an already rare disease, however international collaborative trials groups (such as those in HERBY represent), already recruit hypermutator and MAPK-altered HGGs in this population for appropriately targeted therapies (NCT02992964, NCT02684058). Equally importantly, the histone H3 mutant subgroups which represent a substantial proportion of patients in this age group (Mackay et al., 2017) were found to be very poorly immunogenic, confirming a previous study in resectable malignant brainstem gliomas in children and adults with K27M mutations (Zhang et al., 2017), and further negating the likelihood of clinical response to such therapies.

A key observation is the high prevalence of tumours occurring outside the cerebral hemispheres harbouring histone mutations, included in the most recent 2016 WHO classification system as a novel entity called *diffuse midline glioma with H3K27M mutation.* These represented 27% of the assessed population, and had a particularly poor outcome, as did histone wild-type midline cases. These tumours only rarely have *MGMT* promoter methylation, and have consistently proved refractory to TMZ and other chemotherapeutic agents (Jones et al., 2016). Critically, midline K27M tumours classified histologically as either grade 3 or 4 according to the WHO2007 classification had no difference in clinical outcome within the HERBY cohort, and with the caveat of small numbers, support the current 2016 guidelines to assign all such tumours as grade 4 on the basis of their location and molecular findings.

More surprising was the poor outcome observed for patients with H3F3A_G34R/V mutations. A previous study reported G34R mutations to convey a better prognosis in respect of overall survival (HR 0.49, p=0.01), though this was not significant in multivariate analysis (p=0.84) (Korshunov et al., 2015), although the present study is the first study to explore this in a consistently treated and well-annotated clinical trial setting. In the HERBY study as well in published work (Korshunov et al., 2015; Mackay et al., 2017), H3F3A_G34R/V mutation is associated with a high frequency of *MGMT* methylation. Notably, *MGMT* promoter methylation itself was not predictive in this trial cohort of all patients receiving radiochemotherapy with temozolomide, again demonstrating differences with the adult disease, and questioning the continued use of protocols extrapolated from the adult setting. It is clear that histone mutations represent clearly-defined entities within an umbrella HGG classification in the paediatric setting, and given their profound impact on chromatin modifications, will require novel therapeutic development and clinical trials distinct from histone wild-type cases.

Within the remaining cases of paediatric HGG were a small proportion whose methylation profiles were more similar to other lesions. The LGG-like cases were in young patients with

longer EFS, whilst two additional cases had methylation classifier scores strongly suggestive of newly-described entities coming from the study of tumours formally diagnosed as CNS primitive neuroectodermal tumours (CNS-PNET) (Sturm et al., 2016). Integration with histological features and determination of the presence of marker gene fusions events for these entities (CNS HGNET-MN1, CNS NB-FOXR2) will be key in future studies.

Although there have been several early phase and anecdotal studies of BEV in paediatric HGG (Benesch et al., 2008; Friedman et al., 2013; Gururangan et al., 2010; Narayana et al., 2010; Salloum et al., 2015), none have included biological information on the patients treated. Aside from CD8 immunoreactivity, we did not identify any additional molecular markers of response. In similarly-designed adult studies of BEV, gene expression-defined proneural (Sandmann et al., 2015) or mesenchymal (Sulman et al., 2013) subgroups of GBM have been reported to confer a significant OS advantage. Although we have not undertaken gene expression studies across our cohort, adult and paediatric cases expressing proneural genes appear to have distinct genetic and epigenetic drivers (Sturm et al., 2012), the mesenchymal subclass is rare in children (Sturm et al., 2012), and unlike the adult studies, we observed no EFS advantage of BEV in HERBY (Grill et al., 2018).

In conclusion, integrated molecular profiling of the HERBY sample cohort has demonstrated the biological and clinicopathological diversity of the term HGG in the paediatric setting, suspected but not confirmed at the onset of the trial. Whilst there are several distinct subgroups for which there is strong rationale for bespoke future clinical studies, a large proportion of paediatric HGG cases continue to defy improvements in survival and lack a clear path forward. Although BEV was not associated with better outcome in this trial, the extensive biological, pathological and radiological ancillary research programmes ongoing within HERBY aim to provide an integrated assessment of disease pathogenesis and treatment response.

Acknowledgements:

The HERBY clinical trial was carried out as a collaboration between the European Innovative Therapies for Children with Cancer (ITCC) consortium, the SIOPE Brain Tumour Group, the Australian Children's Cancer Trials Group (ACCT), and the C-17 Council (Canada). The translational research study was funded by an unrestricted grant from F. Hoffmann-La Roche Ltd allied to the HERBY trial (study number BO25041; clinicaltrials.gov NCT01390948). The funder provided infrastructure for sample acquisition, shipping, storage, and record-keeping. The funder had no role in study design, data collection, data analysis, data interpretation, or writing of the report. We acknowledge the excellent technical assistance of staff at the Tumour Profiling Unit at the Institute of Cancer Research, London, UK, Sainte-Anne Hospital, Paris, France, and HistoGeneX, Antwerp, Belgium. AM, AB, VM EID and CJ acknowledge NHS funding to the NIHR Biomedical Research Centre at The Royal Marsden and the ICR; TSJ acknowledges NHS funding to the NIHR Biomedical Research Centre at Great Ormond Street Hospital. MLG recognizes the support from the Associazione per la Ricerca sui Tumori Cerebrali del Bambino. We would like to thank the local investigators, pathologists and radiologists who took part in the HERBY study, and the patients and families who consented to inclusion in the translational research programme.

Author Contributions

CJ, PV, JGrill, TW, SMP, RT, MdT and GV conceived the study. AM, JB-V and CJ analysed data. AB, VM, DTWJ, DC and EID performed molecular analysis. DR, PSM, and TJ carried out radiological analysis. FG, CH, TP, TSJ, DF-B and PV carried out histopathological analysis. MM, MLG and JGrill provided samples. PR, AJW and AR constructed analytical and visualisation tools and databases. HS and JGarcia provided logistical support. AM and CJ wrote the manuscript. All authors approved the manuscript.

Declaration of interests: CJ received a research grant from F. Hoffmann-La Roche Ltd. CJ, PV, MM, JGrill, GV, DR, PM, and TJ received consultancy fees from F. Hoffmann-La Roche Ltd. FG, CH, TP, TSJ, DF-B and PV received travel reimbursement from F. Hoffmann-La Roche. JB-V, HS and JGarcia are employees of F. Hoffmann-La Roche Ltd. RT and MdT are employees of Genentech.

References

Bautista, F., Paci, A., Minard-Colin, V., Dufour, C., Grill, J., Lacroix, L., Varlet, P., Valteau-Couanet, D., and Geoerger, B. (2014). Vemurafenib in pediatric patients with BRAFV600E mutated high-grade gliomas. Pediatr Blood Cancer *61*, 1101-1103.

Benesch, M., Windelberg, M., Sauseng, W., Witt, V., Fleischhack, G., Lackner, H., Gadner, H., Bode, U., and Urban, C. (2008). Compassionate use of bevacizumab (Avastin) in children and young adults with refractory or recurrent solid tumors. Ann Oncol *19*, 807-813.

Bjerke, L., Mackay, A., Nandhabalan, M., Burford, A., Jury, A., Popov, S., Bax, D. A., Carvalho, D., Taylor, K. R., Vinci, M.*, et al.* (2013). Histone H3.3. mutations drive pediatric glioblastoma through upregulation of MYCN. Cancer Discov *3*, 512-519.

Bouffet, E., Larouche, V., Campbell, B. B., Merico, D., de Borja, R., Aronson, M., Durno, C., Krueger, J., Cabric, V., Ramaswamy, V.*, et al.* (2016). Immune Checkpoint Inhibition for Hypermutant Glioblastoma Multiforme Resulting From Germline Biallelic Mismatch Repair Deficiency. J Clin Oncol *34*, 2206-2211.

Brouwer-Visser, J., Cheng, W. Y., Bauer-Mehren, A., Maisel, D., Lechner, K., Andersson, E., Dudley, J. T., and Milletti, F. (2018). Regulatory T-cell Genes Drive Altered Immune Microenvironment in Adult Solid Cancers and Allow for Immune Contextual Patient Subtyping. Cancer Epidemiol Biomarkers Prev *27*, 103-112.

Capper, D., Jones, D. T. W., Sill, M., Hovestadt, V., Schrimpf, D., Sturm, D., Koelsche, C., Sahm, F., Chavez, L., Reuss, D. E.*, et al.* (2018). DNA methylation-based classification of central nervous system tumours. Nature.

Caretti, V., Sewing, A. C., Lagerweij, T., Schellen, P., Bugiani, M., Jansen, M. H., van Vuurden, D. G., Navis, A. C., Horsman, I., Vandertop, W. P.*, et al.* (2014). Human pontine glioma cells can induce murine tumors. Acta Neuropathol *127*, 897-909.

Cohen, K. J., Pollack, I. F., Zhou, T., Buxton, A., Holmes, E. J., Burger, P. C., Brat, D. J., Rosenblum, M. K., Hamilton, R. L., Lavey, R. S., and Heideman, R. L. (2011). Temozolomide in the treatment of high-grade gliomas in children: a report from the Children's Oncology Group. Neuro Oncol *13*, 317-323.

D'Souza, W. N., Chang, C. F., Fischer, A. M., Li, M., and Hedrick, S. M. (2008). The Erk2 MAPK regulates CD8 T cell proliferation and survival. J Immunol *181*, 7617-7629.

Ebert, P. J. R., Cheung, J., Yang, Y., McNamara, E., Hong, R., Moskalenko, M., Gould, S. E., Maecker, H., Irving, B. A., Kim, J. M.*, et al.* (2016). MAP Kinase Inhibition Promotes T Cell and Anti-tumor Activity in Combination with PD-L1 Checkpoint Blockade. Immunity *44*, 609-621.

Eisenstat, D. D., Pollack, I. F., Demers, A., Sapp, M. V., Lambert, P., Weisfeld-Adams, J. D., Burger, P. C., Gilles, F., Davis, R. L., Packer, R.*, et al.* (2015). Impact of tumor location and pathological discordance on survival of children with midline high-grade gliomas treated on Children's Cancer Group high-grade glioma study CCG-945. J Neurooncol *121*, 573-581.

Elamin, Y. Y., Rafee, S., Toomey, S., and Hennessy, B. T. (2015). Immune effects of bevacizumab: killing two birds with one stone. Cancer Microenviron *8*, 15-21.

Finlay, J. L., Boyett, J. M., Yates, A. J., Wisoff, J. H., Milstein, J. M., Geyer, J. R., Bertolone, S. J., McGuire, P., Cherlow, J. M., Tefft, M., and et al. (1995). Randomized phase III trial in childhood high-grade astrocytoma comparing vincristine, lomustine, and prednisone with the eight-drugs-in-1-day regimen. Childrens Cancer Group. J Clin Oncol *13*, 112-123.

Fonov, V., Evans, A. C., Botteron, K., Almli, C. R., McKinstry, R. C., Collins, D. L., and Brain Development Cooperative, G. (2011). Unbiased average age-appropriate atlases for pediatric studies. Neuroimage *54*, 313-327.

Friedman, G. K., Spiller, S. E., Harrison, D. K., Fiveash, J. B., and Reddy, A. T. (2013). Treatment of children with glioblastoma with conformal radiation, temozolomide, and bevacizumab as adjuncts to surgical resection. J Pediatr Hematol Oncol *35*, e123-126.

Gabrilovich, D. I., Chen, H. L., Girgis, K. R., Cunningham, H. T., Meny, G. M., Nadaf, S., Kavanaugh, D., and Carbone, D. P. (1996). Production of vascular endothelial growth factor by human tumors inhibits the functional maturation of dendritic cells. Nat Med *2*, 1096-1103.

Gilles, F. H., Tavare, C. J., Becker, L. E., Burger, P. C., Yates, A. J., Pollack, I. F., and Finlay, J. L. (2008). Pathologist interobserver variability of histologic features in childhood brain tumors: results from the CCG-945 study. Pediatr Dev Pathol *11*, 108-117.

Grill, J., Massimino, M., Bouffet, E., Azizi, A. A., McCowage, G., Canete, A., Saran, F., Le Deley, M. C., Varlet, P., Morgan, P. S.*, et al.* (2018). Phase II, Open-Label, Randomized, Multicenter Trial (HERBY) of Bevacizumab in Pediatric Patients With Newly Diagnosed High-Grade Glioma. J Clin Oncol, JCO2017760611.

Gururangan, S., Chi, S. N., Young Poussaint, T., Onar-Thomas, A., Gilbertson, R. J., Vajapeyam, S., Friedman, H. S., Packer, R. J., Rood, B. N., Boyett, J. M., and Kun, L. E. (2010). Lack of efficacy of bevacizumab plus irinotecan in children with recurrent malignant glioma and diffuse brainstem glioma: a Pediatric Brain Tumor Consortium study. J Clin Oncol *28*, 3069-3075.

Hatae, R., Hata, N., Suzuki, S. O., Yoshimoto, K., Kuga, D., Murata, H., Akagi, Y., Sangatsuda, Y., Iwaki, T., Mizoguchi, M., and Iihara, K. (2016). A comprehensive analysis identifies BRAF hotspot mutations associated with gliomas with peculiar epithelial morphology. Neuropathology.

Hu-Lieskovan, S., Mok, S., Homet Moreno, B., Tsoi, J., Robert, L., Goedert, L., Pinheiro, E. M., Koya, R. C., Graeber, T. G., Comin-Anduix, B., and Ribas, A. (2015). Improved antitumor activity of immunotherapy with BRAF and MEK inhibitors in BRAF(V600E) melanoma. Sci Transl Med *7*, 279ra241.

Jakacki, R. I., Cohen, K. J., Buxton, A., Krailo, M. D., Burger, P. C., Rosenblum, M. K., Brat, D. J., Hamilton, R. L., Eckel, S. P., Zhou, T.*, et al.* (2016). Phase 2 study of concurrent radiotherapy and temozolomide followed by temozolomide and lomustine in the treatment of children with high-grade glioma: a report of the Children's Oncology Group ACNS0423 study. Neuro Oncol *18*, 1442-1450.

Jenkinson, M., Bannister, P., Brady, M., and Smith, S. (2002). Improved optimization for the robust and accurate linear registration and motion correction of brain images. Neuroimage *17*, 825-841.

Jones, C., and Baker, S. J. (2014). Unique genetic and epigenetic mechanisms driving paediatric diffuse high-grade glioma. Nat Rev Cancer *14*.

Jones, C., Karajannis, M. A., Jones, D. T., Kieran, M. W., Monje, M., Baker, S. J., Becher, O. J., Cho, Y. J., Gupta, N., Hawkins, C.*, et al.* (2016). Pediatric high-grade glioma: biologically and clinically in need of new thinking. Neuro Oncol.

Karremann, M., Gielen, G. H., Hoffmann, M., Wiese, M., Colditz, N., Warmuth-Metz, M., Bison, B., Claviez, A., van Vuurden, D. G., von Bueren, A. O.*, et al.* (2018). Diffuse high-grade gliomas with H3 K27M mutations carry a dismal prognosis independent of tumor location. Neuro Oncol *20*, 123-131.

Khuong-Quang, D. A., Buczkowicz, P., Rakopoulos, P., Liu, X. Y., Fontebasso, A. M., Bouffet, E., Bartels, U., Albrecht, S., Schwartzentruber, J., Letourneau, L.*, et al.* (2012). K27M mutation in histone H3.3 defines clinically and biologically distinct subgroups of pediatric diffuse intrinsic pontine gliomas. Acta Neuropathol *124*, 439-447.

Kmiecik, J., Poli, A., Brons, N. H., Waha, A., Eide, G. E., Enger, P. O., Zimmer, J., and Chekenya, M. (2013). Elevated CD3+ and CD8+ tumor-infiltrating immune cells correlate with prolonged survival in glioblastoma patients despite integrated immunosuppressive mechanisms in the tumor microenvironment and at the systemic level. J Neuroimmunol *264*, 71-83.

Korshunov, A., Ryzhova, M., Hovestadt, V., Bender, S., Sturm, D., Capper, D., Meyer, J., Schrimpf, D., Kool, M., Northcott, P. A.*, et al.* (2015). Integrated analysis of pediatric glioblastoma reveals a subset of biologically favorable tumors with associated molecular prognostic markers. Acta Neuropathol *129*, 669-678.

Mackay, A., Burford, A., Carvalho, D., Izquierdo, E., Fazal-Salom, J., Taylor, K. R., Bjerke, L., Clarke, M., Vinci, M., Nandhabalan, M.*, et al.* (2017). Integrated Molecular Meta-Analysis of 1,000 Pediatric High-Grade and Diffuse Intrinsic Pontine Glioma. Cancer Cell *32*, 520-537 e525.

Narayana, A., Kunnakkat, S., Chacko-Mathew, J., Gardner, S., Karajannis, M., Raza, S., Wisoff, J., Weiner, H., Harter, D., and Allen, J. (2010). Bevacizumab in recurrent high-grade pediatric gliomas. Neuro Oncol *12*, 985-990.

Ostrom, Q. T., Gittleman, H., Fulop, J., Liu, M., Blanda, R., Kromer, C., Wolinsky, Y., Kruchko, C., and Barnholtz-Sloan, J. S. (2015). CBTRUS Statistical Report: Primary Brain and Central Nervous System Tumors Diagnosed in the United States in 2008-2012. Neuro Oncol *17 Suppl 4*, iv1-iv62.

Palma, L., Di Lorenzo, N., and Guidetti, B. (1978). Lymphocytic infiltrates in primary glioblastomas and recidivous gliomas. Incidence, fate, and relevance to prognosis in 228 operated cases. J Neurosurg *49*, 854-861.

Paugh, B. S., Qu, C., Jones, C., Liu, Z., Adamowicz-Brice, M., Zhang, J., Bax, D. A., Coyle, B., Barrow, J., Hargrave, D.*, et al.* (2010). Integrated molecular genetic profiling of pediatric high-grade gliomas reveals key differences with the adult disease. J Clin Oncol *28*, 3061-3068.

Pollack, I. F., Boyett, J. M., Yates, A. J., Burger, P. C., Gilles, F. H., Davis, R. L., Finlay, J. L., and Children's Cancer, G. (2003a). The influence of central review on outcome associations in childhood malignant gliomas: results from the CCG-945 experience. Neuro Oncol *5*, 197-207.

Pollack, I. F., Finkelstein, S. D., Burnham, J., Hamilton, R. L., Yates, A. J., Holmes, E. J., Boyett, J. M., and Finlay, J. L. (2003b). Association between chromosome 1p and 19q loss and outcome in pediatric malignant gliomas: results from the CCG-945 cohort. Pediatr Neurosurg *39*, 114-121.

Pollack, I. F., Finkelstein, S. D., Woods, J., Burnham, J., Holmes, E. J., Hamilton, R. L., Yates, A. J., Boyett, J. M., Finlay, J. L., Sposto, R., and Children's Cancer, G. (2002). Expression of p53 and prognosis in children with malignant gliomas. N Engl J Med *346*, 420-427.

Pollack, I. F., Hamilton, R. L., Burger, P. C., Brat, D. J., Rosenblum, M. K., Murdoch, G. H., Nikiforova, M. N., Holmes, E. J., Zhou, T., Cohen, K. J.*, et al.* (2010a). Akt activation is a common event in pediatric malignant gliomas and a potential adverse prognostic marker: a report from the Children's Oncology Group. J Neurooncol *99*, 155-163.

Pollack, I. F., Hamilton, R. L., Sobol, R. W., Burnham, J., Yates, A. J., Holmes, E. J., Zhou, T., and Finlay, J. L. (2006). O6-methylguanine-DNA methyltransferase expression strongly correlates with outcome in childhood malignant gliomas: results from the CCG-945 Cohort. J Clin Oncol *24*, 3431-3437.

Pollack, I. F., Hamilton, R. L., Sobol, R. W., Nikiforova, M. N., Lyons-Weiler, M. A., LaFramboise, W. A., Burger, P. C., Brat, D. J., Rosenblum, M. K., Holmes, E. J.*, et al.* (2011). IDH1 mutations are common in malignant gliomas arising in adolescents: a report from the Children's Oncology Group. Childs Nerv Syst *27*, 87-94.

Pollack, I. F., Hamilton, R. L., Sobol, R. W., Nikiforova, M. N., Nikiforov, Y. E., Lyons-Weiler, M. A., LaFramboise, W. A., Burger, P. C., Brat, D. J., Rosenblum, M. K.*, et al.* (2010b). Mismatch repair deficiency is an uncommon mechanism of alkylator resistance in pediatric malignant gliomas: a report from the Children's Oncology Group. Pediatr Blood Cancer *55*, 1066-1071.

Robinson, G. W., Orr, B. A., and Gajjar, A. (2014). Complete clinical regression of a BRAF V600E-mutant pediatric glioblastoma multiforme after BRAF inhibitor therapy. BMC Cancer *14*, 258.

Rorden, C., Karnath, H. O., and Bonilha, L. (2007). Improving lesion-symptom mapping. J Cogn Neurosci *19*, 1081-1088.

Rutledge, W. C., Kong, J., Gao, J., Gutman, D. A., Cooper, L. A., Appin, C., Park, Y., Scarpace, L., Mikkelsen, T., Cohen, M. L.*, et al.* (2013). Tumor-infiltrating lymphocytes in glioblastoma are associated with specific genomic alterations and related to transcriptional class. Clin Cancer Res *19*, 4951-4960.

Salloum, R., DeWire, M., Lane, A., Goldman, S., Hummel, T., Chow, L., Miles, L., Sutton, M., Stevenson, C., Fouladi, M., and Leach, J. (2015). Patterns of progression in pediatric patients with high-grade glioma or diffuse intrinsic pontine glioma treated with Bevacizumab-based therapy at diagnosis. J Neurooncol *121*, 591-598.

Sandmann, T., Bourgon, R., Garcia, J., Li, C., Cloughesy, T., Chinot, O. L., Wick, W., Nishikawa, R., Mason, W., Henriksson, R.*, et al.* (2015). Patients With Proneural Glioblastoma May Derive Overall Survival Benefit From the Addition of Bevacizumab to First-Line Radiotherapy and Temozolomide: Retrospective Analysis of the AVAglio Trial. J Clin Oncol *33*, 2735-2744.

Scholz, A., Harter, P. N., Cremer, S., Yalcin, B. H., Gurnik, S., Yamaji, M., Di Tacchio, M., Sommer, K., Baumgarten, P., Bahr, O.*, et al.* (2016). Endothelial cell-derived angiopoietin-2 is a therapeutic target in treatment-naive and bevacizumab-resistant glioblastoma. EMBO Mol Med *8*, 39-57.

Schwartzentruber, J., Korshunov, A., Liu, X. Y., Jones, D. T., Pfaff, E., Jacob, K., Sturm, D., Fontebasso, A. M., Quang, D. A., Tonjes, M.*, et al.* (2012). Driver mutations in histone H3.3 and chromatin remodelling genes in paediatric glioblastoma. Nature *482*, 226-231.

Shlien, A., Campbell, B. B., de Borja, R., Alexandrov, L. B., Merico, D., Wedge, D., Van Loo, P., Tarpey, P. S., Coupland, P., Behjati, S.*, et al.* (2015). Combined hereditary and somatic mutations of replication error repair genes result in rapid onset of ultra-hypermutated cancers. Nat Genet *47*, 257-262.

Sturm, D., Orr, B. A., Toprak, U. H., Hovestadt, V., Jones, D. T., Capper, D., Sill, M., Buchhalter, I., Northcott, P. A., Leis, I.*, et al.* (2016). New Brain Tumor Entities Emerge from Molecular Classification of CNS-PNETs. Cell *164*, 1060-1072.

Sturm, D., Witt, H., Hovestadt, V., Khuong-Quang, D. A., Jones, D. T., Konermann, C., Pfaff, E., Tonjes, M., Sill, M., Bender, S.*, et al.* (2012). Hotspot mutations in H3F3A and IDH1 define distinct epigenetic and biological subgroups of glioblastoma. Cancer Cell *22*, 425-437.

Sulman, E. P., Won, M., Blumenthal, D. T., Vogelbaum, M. A., Colman, H., Jenkins, R. B., Chakravarti, A., Jeraj, R., Brown, P. D., Jaeckle, K. A.*, et al.* (2013). Molecular predictors of outcome and response to bevacizumab (BEV) based on analysis of RTOG 0825, a phase III trial comparing chemoradiation (CRT) with and without BEV in patients with newly diagnosed glioblastoma (GBM). J Clin Oncol *31*, abstr LBA2010.

Wallin, J. J., Bendell, J. C., Funke, R., Sznol, M., Korski, K., Jones, S., Hernandez, G., Mier, J., He, X., Hodi, F. S.*, et al.* (2016). Atezolizumab in combination with bevacizumab enhances antigen-specific T-cell migration in metastatic renal cell carcinoma. Nat Commun *7*, 12624.

Wilmott, J. S., Long, G. V., Howle, J. R., Haydu, L. E., Sharma, R. N., Thompson, J. F., Kefford, R. F., Hersey, P., and Scolyer, R. A. (2012). Selective BRAF inhibitors induce marked T-cell infiltration into human metastatic melanoma. Clin Cancer Res *18*, 1386-1394.

Wu, G., Broniscer, A., McEachron, T. A., Lu, C., Paugh, B. S., Becksfort, J., Qu, C., Ding, L., Huether, R., Parker, M.*, et al.* (2012). Somatic histone H3 alterations in pediatric diffuse intrinsic pontine gliomas and non-brainstem glioblastomas. Nat Genet *44*, 251-253.

Wu, G., Diaz, A. K., Paugh, B. S., Rankin, S. L., Ju, B., Li, Y., Zhu, X., Qu, C., Chen, X., Zhang, J.*, et al.* (2014). The genomic landscape of diffuse intrinsic pontine glioma and pediatric non-brainstem high-grade glioma. Nat Genet *46*, 444-450.

Zhang, Y., Pan, C., Wang, J., Cao, J., Liu, Y., Wang, Y., and Zhang, L. (2017). Genetic and immune features of resectable malignant brainstem gliomas. Oncotarget *8*, 82571-82582.

Legends for Figures

Figure 1 – *Sample cohort.* (A) Flow diagram indicating total HERBY trial cohort (n=121 randomised plus 3 infants), those patients consenting to the biology study (n=113) for whom sufficient FFPE or frozen tumour was available (n=89), and the respective molecular analyses undertaken. Kaplan-Meier plots of event-free survival of cases (y axis) separated by (B) treatment arm, (C) anatomical location, or (D) *H3F3A* status, with time given in months (x axis) and p value calculated by the log-rank test. See also Table S1.

Figure 2 - *Methylation-based subclassification.* (A) Heatmap representation of beta values for 74 samples profiled on the Illumina 450k BeadArray platform (red, high; blue, low). Samples are arranged in columns clustered by probes with the largest median absolute deviation across the 10k predictor subset of probes. Clinicopathological and molecular annotations are provided as bars according to the included key. CR/PR = complete response or partial response; Stable/NC = stable disease or no change. (B) Boxplot showing age at diagnosis of included cases, separated by methylation subclass. Kaplan-Meier plot of (C) event-free and overall survival of cases (y axis) separated by methylation subclass, time given in months (x axis) and overall p value calculated by the log-rank test. See also Figures S1, S2, S3 and Table S1.

Figure 3 – *Somatic mutations*. (A) Oncoprint representation of an integrated annotation of somatic mutations and DNA copy number changes for the 30 most frequently altered genes in 86 samples ($n \geq 3$, frequency barplot on the right, excluding hypermutator cases). Selected common fusion events are also shown where available. Samples are arranged in columns with genes labelled along rows. (B) Barplots are provided on a $\log_{10}$ scale for numbers of copy number aberrations and somatic mutations per case. Clinicopathological and molecular annotations are provided as bars according to the included key. CR/PR = complete response

or partial response; Stable/NC = stable disease or no change. See also Figure S4 and Table S1.

Figure 4 – *H3F3A mutant subgroups*. (A) Integrated annotation of somatic mutations and DNA copy number changes in 7 H3F3A_G34R/V cases. (B) H&E (top) and immunohistochemistry (bottom) directed against H3.3G34R. (C) Radiological tumour lesion map of H3F3A_G34R/V and H3F3A_K27M cases. Brighter coloured pixels indicate a higher probability of tumour incidence. (D) Kaplan-Meier plot of event-free and overall survival of hemispheric cases (y axis) separated by *H3F3A* status, time given in months (x axis), p value calculated by the log-rank test. (E) Integrated data from 21 H3F3A_K27M cases. (F) H&E (top) and immunohistochemistry (bottom) directed against H3.3K27M. (G) Kaplan-Meier plot of event-free and overall survival of midline cases (y axis) separated by *H3F3A* status, time given in months (x axis), p value calculated by the log-rank test. See also Figure S5 and Table S1.

Figure 5 – *Hypermutator cases.* (A) Circos plots for four hypermutator cases. In each case, plots provide somatic SNVs and InDels on the outer ring, DNA copy number changes (dark red, amplification; red, gain; dark blue, deletion; blue, loss) and loss of heterozygosity (yellow) on the inner rings, and intra- (orange) and inter- (blue) chromosomal translocations inside the circle. (B) Mutation signatures. (Top) Simple stacked barplot representation of the proportion of mutation types observed in individual hypermutator cases and the remaining accumulated dataset. Base changes given in the key. (Bottom) Mutation context given for each of the 96 mutated trinucleotides, represented by heatmap. The base located 5′ to each mutated base is shown on the vertical axis, and the 3′ base is on the horizontal axis. (C) (Top) H&E and (bottom) protein expression of mismatch repair proteins MLH1, MSH2, MSH6 and PMS2 as assessed by immunohistochemistry in a glioblastoma with 5322 somatic mutations (HERBY102). (D) CD8 expression in T cells by immunohistochemistry in HERBY102 (E) Boxplot of percentage of $CD8^+$ cells in the central tumour region separated by subgroup. *** $p<0.0001$, t-test. See also Table S1.

Figure 6 – *PXA-like tumours*. (A) Integrated annotation of somatic mutations and DNA copy number changes in 9 samples classifying as PXA-like. (B) Haematoxylin and eosin staining of an epithelioid (top) and giant cell (bottom) variant of glioblastoma. (C) CD8 immunohistochemistry for the same cases as (B), marking $CD8^+$ T cells. (D) Radiological tumour lesion map of PXA-like cases. Brighter coloured pixels indicate a higher probability of tumour incidence. See also Table S1.

Figure 7 – *Immune signatures and response to bevacizumab.* (A) Mean T effector / T cell gene expression values (plotted as $\log_2$, x axis) data were correlated with CD8 immunoreactivity (plotted as $\log_{10}$, y axis). Two cases were scored as 0% by IHC and were not plotted (expression values -7.37 and -7.58). (B) Gene expression signatures for CD8 T effector and T cells plotted as a heatmap from RNAseq data. Hypermutator cases and those with MAPK alterations including *NF1*, *FGFR1* or *NTRK2* are annotated. (C) Boxplot of T effector / T cell gene expression values in MAPK altered samples compared to those without. Bold line represents the median, whiskers span the interquartile range. (D) Kaplan-Meier plot of event-free and overall survival of cases (y axis) treated with TMZ/RT, separated by levels of $CD8^+$ T cells, time given in months (x axis) and p value calculated by the log-rank test. (E) TMZ/RT plus BEV, separated by levels of $CD8^+$ T cells, time given in months (x axis) and p value calculated by the log-rank test. See also Figures S6-S7 and Table S1.

STAR Methods

CONTACT FOR REAGENT AND RESOURCE SHARING

Further information and requests for resources and reagents should be directed to and will be fulfilled by the Lead Contact, Chris Jones (chris.jones@icr.ac.uk).

EXPERIMENTAL MODEL AND SUBJECT DETAILS

Patient samples

All patient samples were collected after signed consent to the HERBY translational research program, under full Research Ethics Committee approval at each participating centre. Tumour material was available from 89 patients (out of a total of 113 providing consent) from 13 countries (France n=27, UK n=17, Italy n=14, Spain n=6, Canada n=5, Netherlands n=4, Czech Republic n=3, Denmark n=3, Hungary n=3, Sweden n=3, Poland n=2, Austria n=1, Belgium n=1).

Pathological review

All patients had their initial local diagnosis of HGG confirmed according to the WHO 2007 classification by a central HERBY reference neuropathologist prior to enrollment. Subsequently, all specimens were further subjected to a consensus review by the HERBY panel of five independent expert paediatric neuropathologists, who also applied the diagnostic criteria of the WHO 2016 classification.

Radiological anatomical localization

Tumour localization was determined by the HERBY panel of paediatric neuroradiologists. Tumours were assigned to lobar, basal ganglia, thalamic, non-pontine brainstem or cerebellar locations. As many of the tumours spanned more than one of these locations, post hoc radiological analysis by one of the HERBY Neuroradiologists was undertaken to determine

the epicentre of the tumour origin; this was used to classify the site of origin of the tumour in each case.

METHOD DETAILS

Nucleic acid extraction

DNA was extracted from frozen tissue by homogenisation prior to following the DNeasy Blood & Tissue kit protocol (Qiagen, Crawley, UK). DNA was extracted from formalin-fixed, paraffin-embedded (FFPE) pathology blocks after manual macrodissection using the QIAamp DNA FFPE tissue kit protocol (Qiagen). Matched normal DNA was extracted from blood samples using the DNeasy Blood & Tissue kit (Qiagen, Crawley, UK). Concentrations were measured using a Qubit fluorometer (Life Technologies, Paisley, UK). RNA was extracted by following the RNeasy Mini Kit protocol (Qiagen), and quantified on a 2100 Bioanalyzer (Agilent Technologies).

H3F3A Sanger sequencing

PCR for *H3F3A* was carried out on 89 cases using primers obtained from Life Technologies (Paisley, UK) (FFPE: for-TGGCTCGTACAAAGCAGACT; rev-ATATGGATACATACAAGAGAGACT; FROZEN: for-GATTTTGGGTAGACGTAATCTTCA; rev-TTTCCTGTTATCCATCTTTTTGTT). Sequences were analysed using Mutation Surveyor (SoftGenetics, PN, USA) and manually with 4Peaks (Nucleobytes, Aalsmeer, Netherlands). Only three cases left insufficient DNA for exome sequencing, all of which were found to harbour K27M mutations, and thus additional Sanger sequencing for genes encoding H3.1 variants were not undertaken.

Methylation profiling

50-500ng DNA was bisulphite-modified and analyzed for genome-wide methylation patterns using the Illumina HumanMethylation450 BeadArray (450k) platform at either the DKFZ or the University College London Genomics Centre, according the manufacturers instructions. All

samples were checked for expected and unexpected genotype matches by pairwise correlation of the 65 genotyping probes on the 450k array.

MGMT promoter methylation

To evaluate the methylation status of the *MGMT* promoter region, we used either the MGMT_STP27 logistic regression model from Illumina 450k methylation array data, or methylation-specific (MS-) PCR. For MS-PCR, 300-1500ng DNA was sodium bisulphite-treated and PCR products analyzed on an the ABI7900HT instrument (Applied Biosystems, Foster City, CA, USA) to quantify the copy number of MGMT/ACTB (MDxHealth, Irvine, CA, USA).

Next-generation sequencing

50-500ng DNA from 86 cases was sent for exome sequencing at the Tumour Profiling Unit (ICR, London, UK) using the Agilent SureSelectXT Human All Exon V6 platform with additional customized coverage of all histone H3 genes and the *TERT* promoter (Agilent, Santa Clara, CA, USA), and paired-end-sequenced on an Illumina HiSeq2500 (Illumina, San Diego, CA, USA) with one single patient-matched tumour/normal pair per lane where possible. The average median coverage was 426x for the frozen tumours (range 351-598x), 321x for the FFPE tumours (range 115-519x) and 163x for normal samples (range 116-464x). A customized panel of biotinylated DNA probes (NimbleGen) was developed for the detection of structural variants (translocations and duplications) and potential amplifications. The panel capture a total of 22 genes recently implicated in brain tumours (*ALK, BCOR, BRAF, c11orf95, C19MC, CIC, ETV6, FGFR1-3, FOXR2, KIAA1549, MET, MN1, MYB, MYBL1, NTRK1-3, RAF, RELA, TPM3* and *YAP1*). Library preparation was performed using 50-200 ng of genomic DNA using the HyperPlus Kit (Kapa Biosystems, Wilmington MA, USA) and SeqCap EZ adapters (Roche). Following fragmentation, DNA was end-repaired, A-tailed and indexed adapters ligated. DNA was amplified, multiplexed and hybridized using 1 µg of total pre-capture library DNA to the design of DNA baits (NimbleGen SeqCap EZ Developer library, Roche). After hybridization, capture libraries were amplified and sequencing was performed

on a NextSeq500 (Illumina) with 2 x 150bp, paired-end reads following manufacturer's instructions. RNA from frozen tumours was sequenced on an Illumina HiSeq2500 as 100bp paired end reads.

Immunohistochemistry

4µM sections were stained by an automated Discovery XT (for H3G34R) or Benchmark XT (Ventana Medical Systems, Tucson, USA). A standard pre-treatment protocol included CC1 buffer (or CC2 for H3G34R) and then a primary antibody incubation for 32 minutes (92 minutes for MLH1, PMS2, MSH2 and MSH6) at room temperature (37°C for H3K27M and MLH1). Antibodies used were directed against MLH1 (BD Pharmingen, clone G168-728, 1/300), PMS2 (BD Pharmingen, clone A16-4, 1/150), MSH2 (DIAG-BIOSYSTEMS, clone 25D12, 1/10), MSH6 (DIAG-BIOSYSTEMS, clone 44, 1/50), H3K27M (Merck, polyclonal, 1/1000), CD8 (Dako, clone C8/144B, 1/100), CD68 (Glostrup, clone KP1, 1/400) and H3G34R (kind gift from Richard Grundy, Children's Brain Tumor Research Centre, Nottingham, UK, polyclonal; 1/150). Antibody binding was visualized with an Optiview Kit (Roche-Ventana, Tucson, USA). Diaminobenzidine-tetra-hydrochloride (DAB, Ventana) was used as the chromogen.

Pathological assessment of immune response

CD8 immunoreactivity was assessed as the percentage of the surface area of the tumour covered by $CD8^+$ cells present at a density belonging to one of four reference bins of increasing density (I0, I1, I2, I3). A further quantitative assessment of the percentage of the pathologist-defined central tumour area of $CD8^+$ cells was also performed. A qualitative categorization of the tumour as a whole as either 'inflamed', 'heterogeneous' or an immune 'desert' was also provided. Patients in the upper quartile of central tumour area CD8 cell positivity with a heterogeneous or inflamed phenotype were classed as CD8-high. A histologically-defined assessment of tumour infiltrating lymphocytes (TILs) was carried out according to two distinct schema. Palma *et al.* (Palma et al., 1978) includes Category A

(several perivascular cuffs of more than three layers of lymphocytes and often lymphocytes also scattered among tumor cells), Category B (three or four thin perivascular cuffs in the tumor) and Category C (no clear lymphocytes present); Rutledge *et al*. (Rutledge et al., 2013) includes Category 0 (absence of lymphocytes), Category 1+ (lymphocytes in less than 50% of the tumor) and Category 2+ (lymphocytes in more than 50% of the tumor).

QUANTIFICATION AND STATISTICAL ANALYSIS

Sequence analysis

Exome capture reads were aligned to the hg19 build of the human genome using bwa v0.7.5a (bio-bwa.sourceforge.net), and PCR duplicates removed with PicardTools 1.5 (pcard.sourceforge.net). Somatic single nucleotide variants were called using the Genome Analysis Tool Kit v3.3-0 based upon current Best Practices using local re-alignment around InDels, downsampling and base recalibration with variants called by the Unified Genotyper (broadinstitute.org/gatk/). Somatic variants were covered by at least 20 reads in both tumour and normal sequences and carried at least 5 ALT reads in the tumour sequence; unmatched exomes (n=3) were annotated by ExAc and ANNOVAR. Variants were annotated using the Ensembl Variant Effect Predictor v74 (ensembl.org/info/docs/variation/vep) incorporating SIFT (sift.jcvi.org) and PolyPhen (genetics.bwh.harvard.edu/pph2) predictions, COSMIC v64 (sanger.ac.uk/ genetics/CGP/cosmic/) and dbSNP build 137 (ncbi.nlm.nih.gov/sites/SNP) annotations. Copy number was obtained by calculating $\log_2$ ratios of tumour/normal coverage binned into exons of known Ensembl genes, smoothed using circular binary segmentation (`DNAcopy`, www.bioconductor.org) and processed using in-house scripts. Mutation signatures were ascertained by grouping somatic substitutions on the basis of their 3′ and 5′ bases into 96 possible trinucleotide categories (Shlien et al., 2015). NGS fusion panel alignment was performed against the human reference sequence GRCh37/Hg19. Quality control (QC), variant annotation, deduplication and metrics were generated for each sample. Manta (https://github.com/Illumina/manta) and Breakdancer (breakdancer.sourceforge.net) were used for the detection of structural variants.

Methylation profiling

Methylation data from the Illumina Infinium HumanMethylation450 BeadChip was preprocessed using the `minfi` package in R. DNA copy number was recovered from combined intensities using the `conumee` package with reference to methylation profiles from normal individuals provided in the `CopyNumber450kData` package. We have used the Heidelberg brain tumour classifier(Capper et al., 2018) (molecularneuropathology.org) to assign subgroup scores for each tumour compared to 91 different brain tumour entities using a training set built from 2801 tumours implemented in the `MNP` R package (v11b2). Simplified methylation subgroup assignments were then made to incorporate cases carrying G34R/V or K27M mutations in H3 histones, IDH1 mutation at R132, low grade glioma-like profiles (predominantly diffuse infantile ganglioglioma and pilocytic astrocytoma) and those similar to pleomorphic xanthoastrocytoma (PXA). Low-scoring cases, or those with a high normal cell contamination were assigned to G34, K27 or IDH1 groups if the respective mutation was identified. Wild-type HGG encompassed many other methylation subgroups and were simply assigned by exclusion with the groups above. Clustering of beta values from methylation arrays was performed using the 10K probeset from the Heidelberg classifier based upon Euclidean distance with a ward algorithm. Methylation heatmaps show only the most variable probes of the classifier between simplified methylation subgroups.

RNAseq

RNA sequences were aligned to hg19 and organised into de-novo spliced alignments using bowtie2 and TopHat version 2.1.0 (ccb.jhu.edu/software/tophat). Fusion transcripts were detected using chimerascan version 0.4.5a filtered to remove common false positives. RNASeq raw count files were used to construct an expression matrix using Roche's internal pipeline. The expression matrix was normalized using edgeR and Voom in R (cran.rproject.org/), and a heatmap was created from the absolute gene expression data using Tibco Spotfire, as previously described (Brouwer-Visser et al., 2018). The mean expression

of the signature genes was used to compare MAPK-altered to non-altered samples and statistical significance calculated using a two-tailed unpaired t-test. The mean expression was also used to correlate with CD8 positivity by IHC. Gene Set enrichment analysis was performed using the GSEA java application based upon pairwise comparisons of MAPK altered *versus* wild-type for curated canonical gene sets. All data are deposited in the European Genome-phenome Archive (ebi.ac.uk/ega/home) under accession number EGAS00001002328.

Tumour lesion maps

Pre-surgery tumour volume regions of interest (ROIs) were drawn on T2-weighted/Fluid-attenuated inversion recovery (FLAIR) magnetic resonance (MR) images by an experienced paediatric neuroradiologist (TJ). The images and corresponding ROIs were affinely registered, using FSL (Jenkinson et al., 2002), to a paediatric template (Left-Right Symmetric, 7.5–13.5 years old) from the Montreal Neurological Institute (http://www.bic.mni.mcgill.ca/ServicesAtlases/NIHPD-obj1) (Fonov et al., 2011). A further manual correction step was performed to limit tumour mass effects. Once registered to a common space, overall tumour lesion overlap maps were created using MRIcron (Rorden et al., 2007).

Statistical analysis

Statistical analysis was carried out using R 3.3.0 (www.r-project.org) and GraphPad Prism 7. Categorical comparisons of counts were carried out using Fishers exact test, comparisons between groups of continuous variables employed Student's t-test or ANOVA. Univariate differences in survival were analysed by the Kaplan-Meier method and significance determined by the log-rank test. Exploratory Cox regression analyses were conducted to assess the impact of molecular prognostic and predictive factors. Confirmation of proportional hazards was assessed by calculating Schoenfeld residuals. All tests were two-sided and a *p* value of less than 0.05 was considered significant.

DATA AND SOFTWARE AVAILABILITY

All newly generated data have been deposited in the European Genome-phenome Archive (www.ebi.ac.uk/ega) with accession number EGAS00001002328 (sequencing) or ArrayExpress (www.ebi.ac.uk/arrayexpress/) with accession number E-MTAB-5552 (450k methylation).

ADDITIONAL RESOURCES

Curated gene-level copy number, mutation data and RNAseq data are provided as part of the paediatric-specific implementation of the cBioPortal genomic data visualization portal (pedcbioportal.org). Raw data files are also made available through the Cavatica NIH-integrated cloud platform (cavatica.org).

Supplemental Tables

Table S1 (related to Figures 1-7) – *Summary of clinicopathological and molecular data.* (A) Sample cohort. (B) Methylation-based subclassification. (C) Focal amplifications and deletions. (D) Chromosomal gains and losses. (E) Somatic single nucleotide variants and small insertions/deletions. (F) Candidate gene fusions.

Table S2 (related to Figure 7) – *Gene set enrichment analysis of MAPK altered versus wild-type paediatric high grade glioma in the HERBY and meta-analysis datasets.* Provided are the names of curated canonical datasets, the enrichment score (ES), normalised enrichment score (NES), the nominal (NOM) p value, the false discovery rate (FDR) q value, the family-wise error rate (FWER) p value and the position in the ranked list at which the maximum enrichment score occurred (RANK AT MAX).

KEY RESOURCES TABLE

REAGENT or RESOURCE	SOURCE	IDENTIFIER
Critical Commercial Assays		
DNeasy blood & tissue kit	Qiagen	69504
QIAmp DNA FFPE tissue kit	Qiagen	56404
RNeasy mini kit	Qiagen	74104
QIAquick PCR purification kit	Qiagen	28104
BigDye terminator v3.1 mix	Thermo Fisher	4337455
SureSelect Human All Exon capture set V6	Agilent	5190-8863
SureSelect RNA Capture, 0.5-2.9Mb	Agilent	5190-4944
Deposited Data		
Exome and RNA sequencing of new samples	This paper	EGA: EGAS00001002328
Illumina methylation BeadChip profiling of new samples	This paper	ArrayExpress: E-MTAB-5552
Sequencing and methylation data	This paper	cavatica.org
Oligonucleotides		
Primer: H3F3A_forward FFPE TGGCTCGTACAAAGCAGACT	This paper	N/A
Primer: H3F3A_reverse FFPE ATATGGATACATACAAGAGAGACT	This paper	N/A
Primer: H3F3A _forward FROZEN GATTTTGGGTAGACGTAATCTTCA	This paper	N/A
Primer: H3F3A _ reverse FROZEN TTTCCTGTTATCCATCTTTTTGTT	This paper	N/A
Antibodies		
MLH1	BD Pharmingen	G168-728
PMS2	BD Pharmingen	A16-4
MSH2	DIAG-BIOSYSTEMS	25D12
MSH6	DIAG-BIOSYSTEMS	44
H3K27M	Merck	ABE419
H3G34R	University of Nottingham	richard.grundy@nottingham.ac.uk
CD8	Dako	C8/144B
CD68	Glostrup	KP1
Software and Algorithms		
Mutation Surveyor	SoftGenetics	softgenetics.com/mutationSurveyor.php
4Peaks	Nucleobytes	nucleobytes.com/4peaks/
minfi	BioConductor	bioconductor.org/packages/release/bioc/html/minfi.html
conumee	BioConductor	bioconductor.org/packages/release/bioc/html/conumee.html
BEDtools	University of Utah	github.com/arq5x/bedtools2

DNAcopy	BioConductor	bioconductor.org/packages/release/bioc/html/DNAcopy.html
CopyNumber450kData	BioConductor	bioconductor.org/packages/release/data/experiment/html/CopyNumber450kData.html
MNP	DKFZ Heidelberg	molecularneuropathology.org/mnp
Bowtie2	Johns Hopkins University	bowtie-bio.sourceforge.net/bowtie2/index.shtml
TopHat	Johns Hopkins University	ccb.jhu.edu/software/tophat/index.shtml
cufflinks	University of Washington	ole-trapnell-lab.github.io/cufflinks/cufflinks/
DESeq2	BioConductor	bioconductor.org/packages/release/bioc/html/DESeq2.html
Gene Set Enrichment Analysis	Broad Institute	http://software.broadinstitute.org/gsea
bwa	Sanger Institute	http://bio-bwa.sourceforge.net/
Genome Analysis Toolkit	Broad Institute	oftware.broadinstitute.org/gatk/
Variant Effect predictor	Ensembl tools	ensembl.org/info/docs/variation/vep
BCBio	Harvard TH Chan	bcb.io/
ANNOVAR	Children's Hospital of Philadelphia	annovar.openbioinformatics.org/en/latest/
ExAc	Broad Institute	exac.broadinstitute.org/
SIFT	J Craig Venter Institute	sift.jcvi.org
PolyPhen	Harvard	genetics.bwh.harvard.edu/pph2
Manta	Illumina	github.com/Illumina/manta
Breakdancer	Washington University of St Louis	breakdancer.sourceforge.net
Oncoprinter	Memorial Sloan Kettering	cbioportal.org/oncoprinter.jsp
Circos	Michael Smith Genome Sciences Center	circos.ca
R	The Comprehensive R Archive Network	r-project.org
Other		
Integrated mutation, copy number, expression and methylation data	This paper and cited sources	pedcbioportal.org

Figure 1

Click here to download Figure
HERBY.biology.Figure.1.FINAL.Mar18.tif

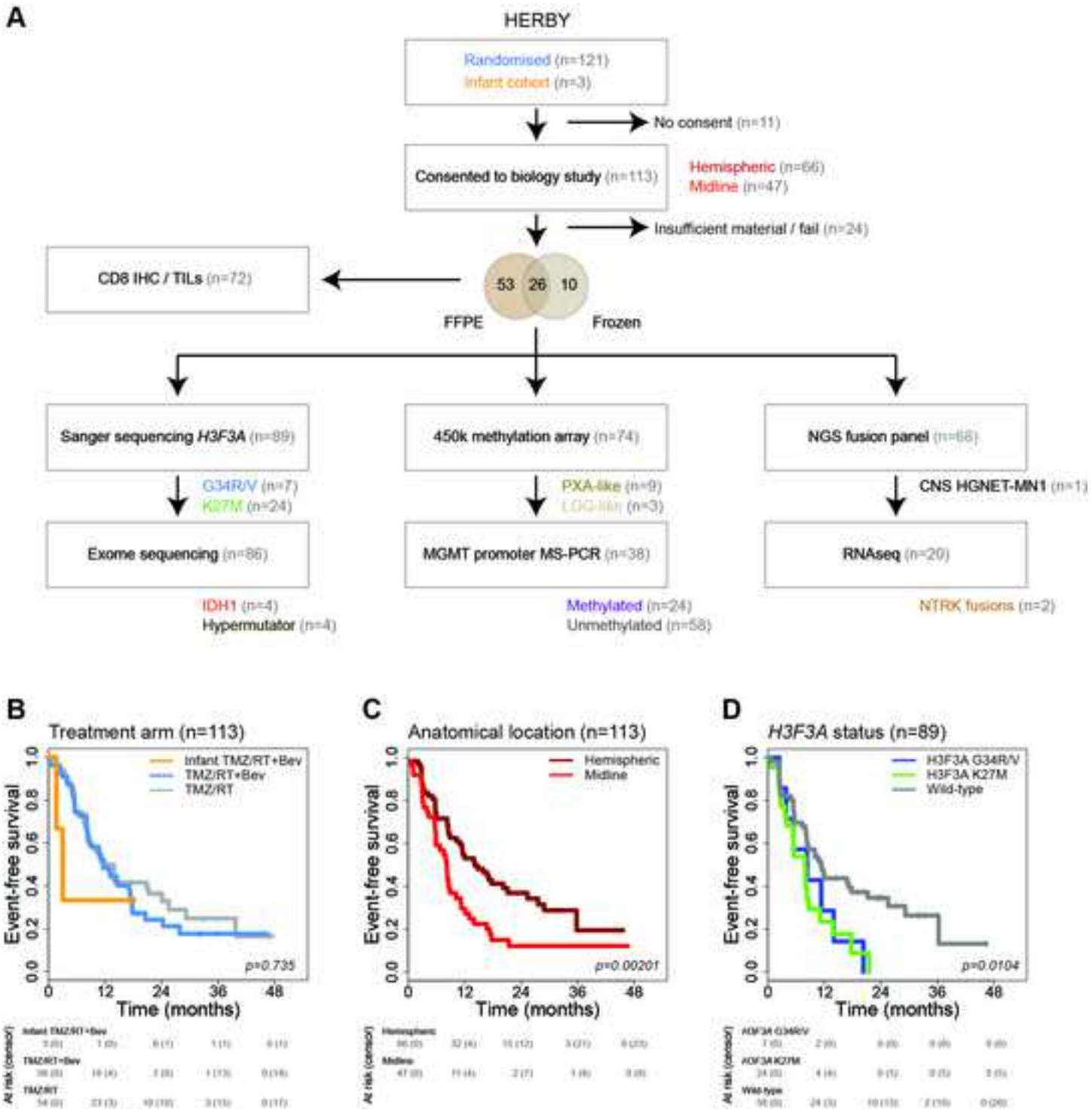

Figure 2

Click here to download Figure
HERBY.biology.Figure.2.FINAL.Mar18.tif

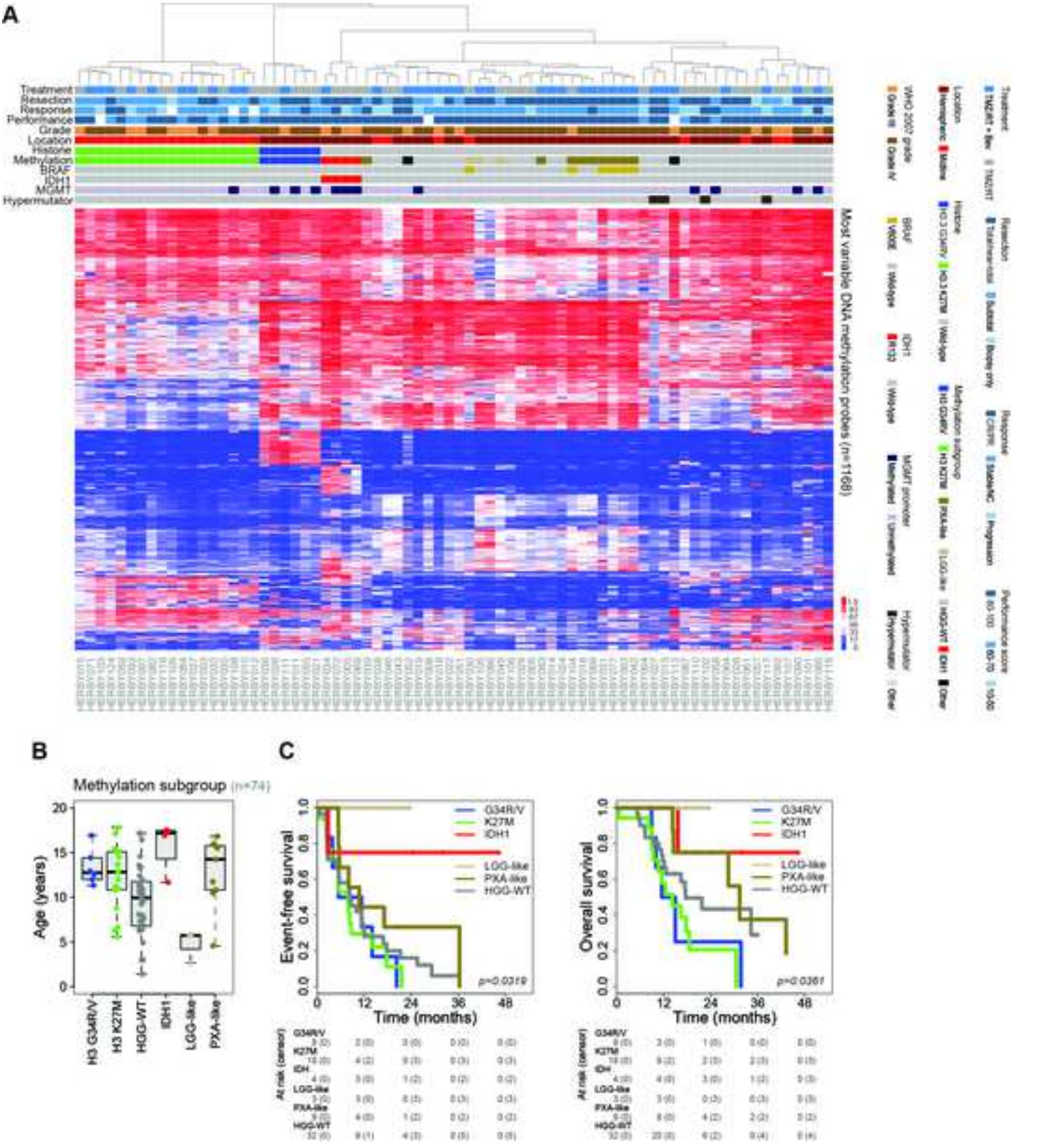

Figure 3

Click here to download Figure HERBY.biology.Figure.3.FINAL.Mar18.tif

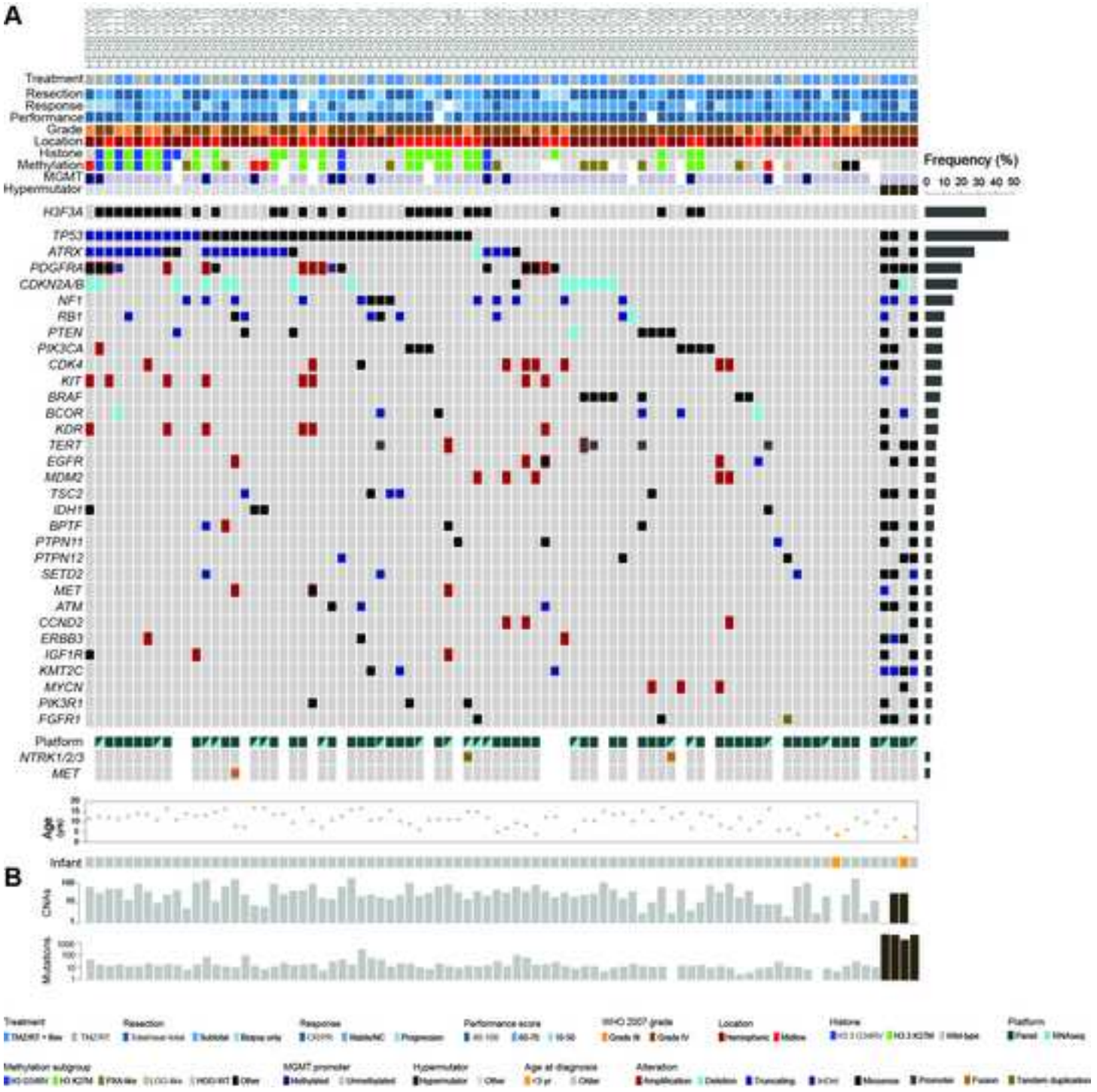

Figure 4

Click here to download Figure
HERBY.biology.Figure.4.FINAL.Mar18.tif

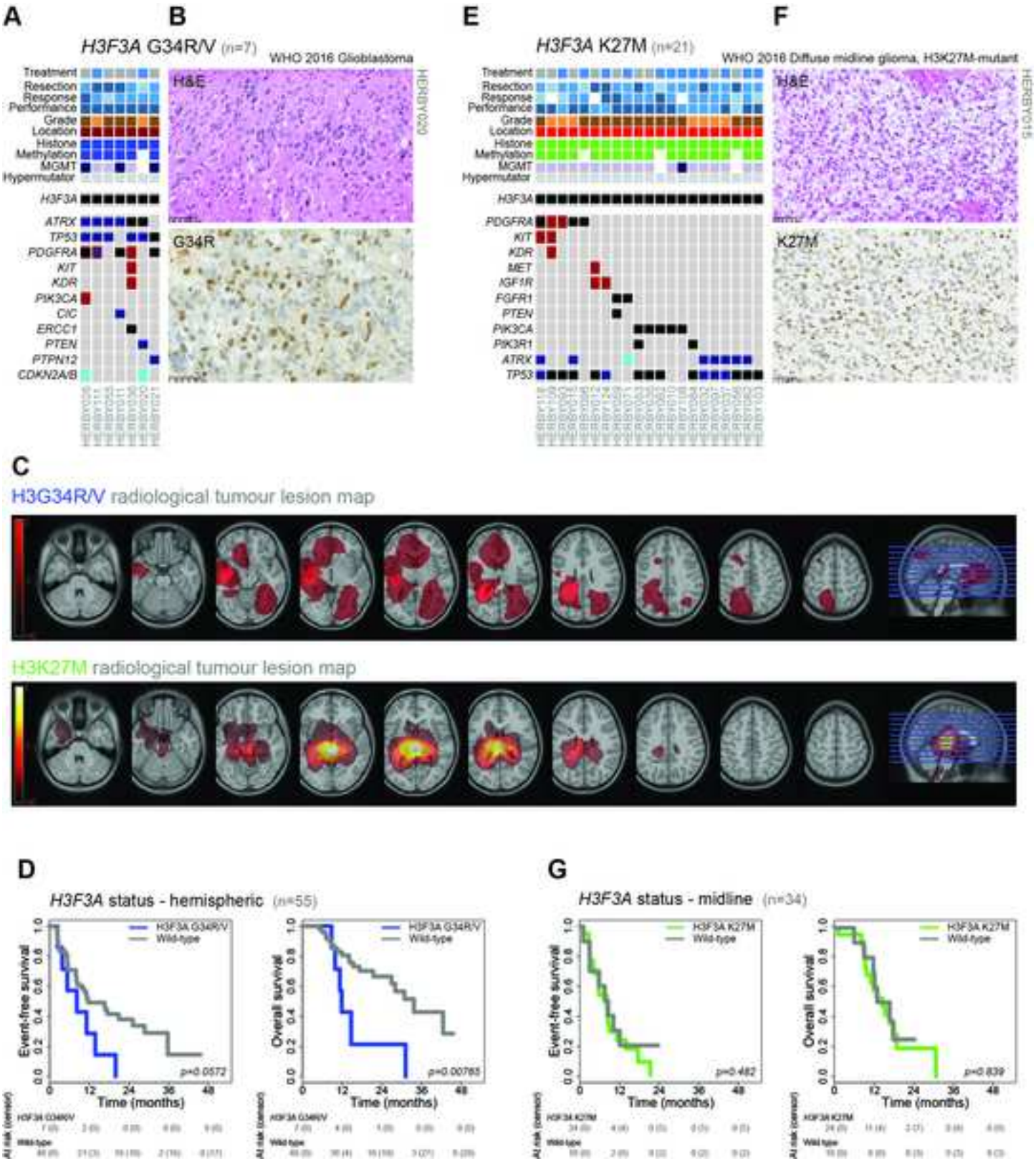

Figure 5

Click here to download Figure HERBY.biology.Figure.5.FINAL.Mar18.tif

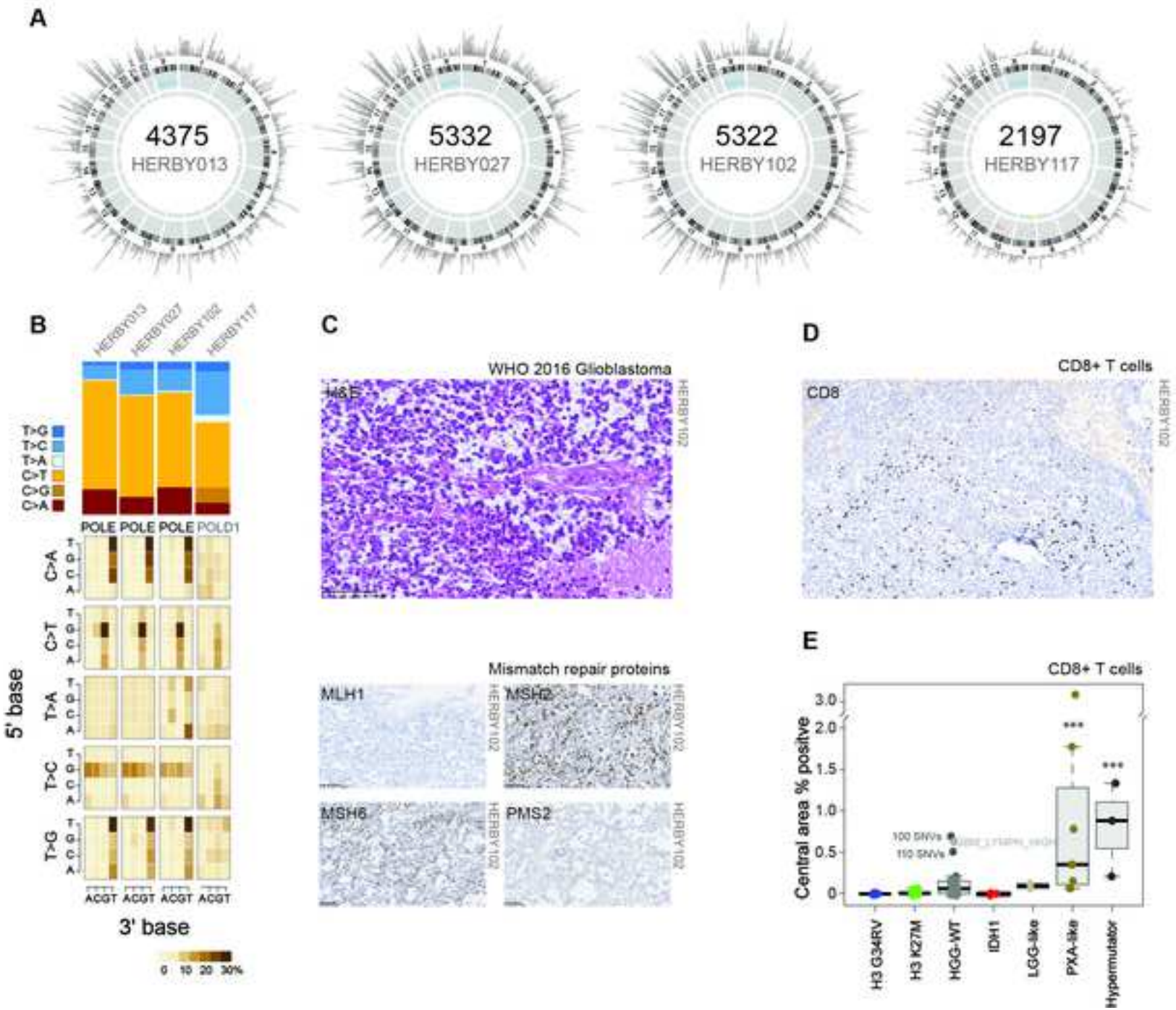

Figure 6

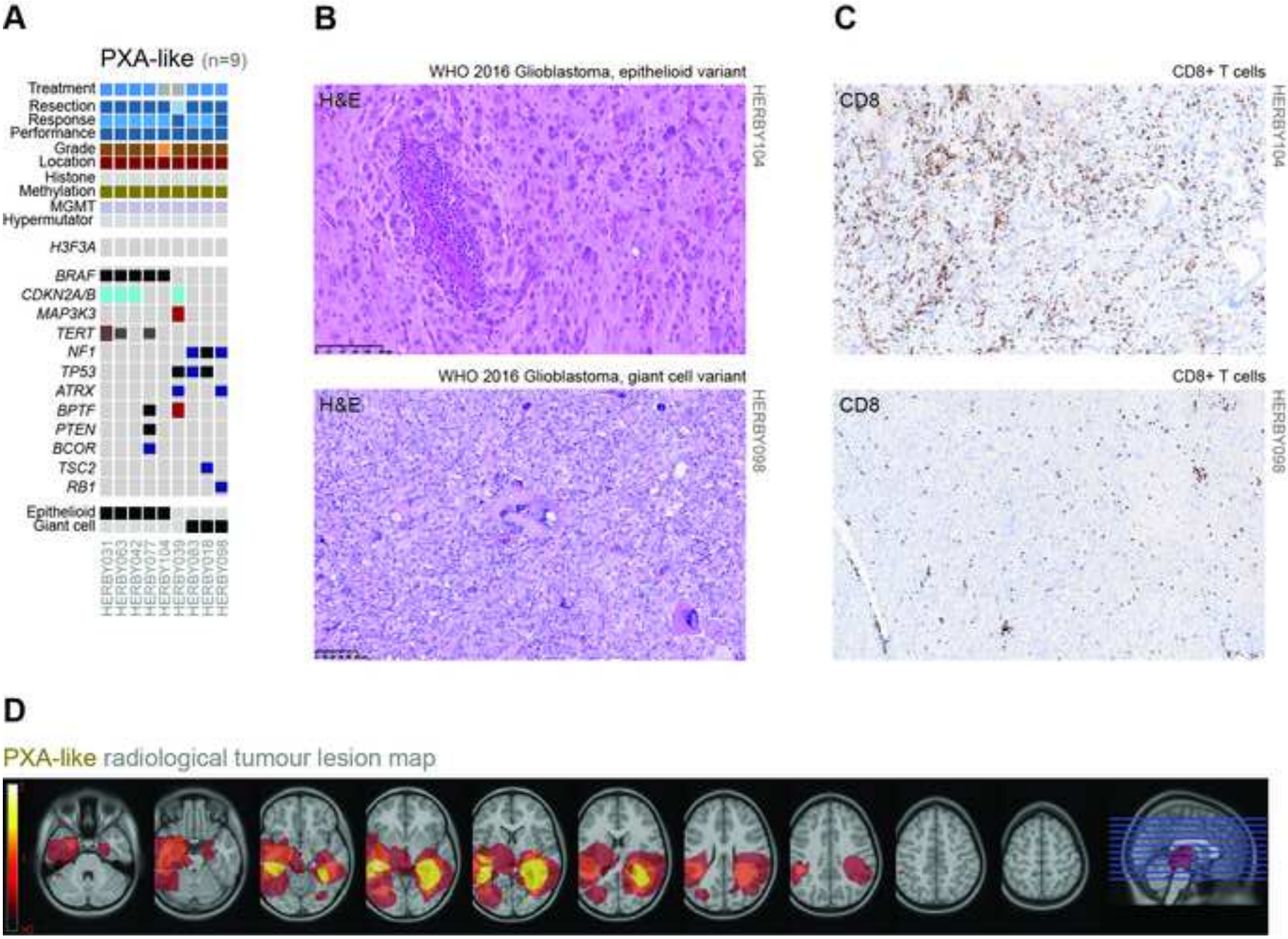

Figure 7

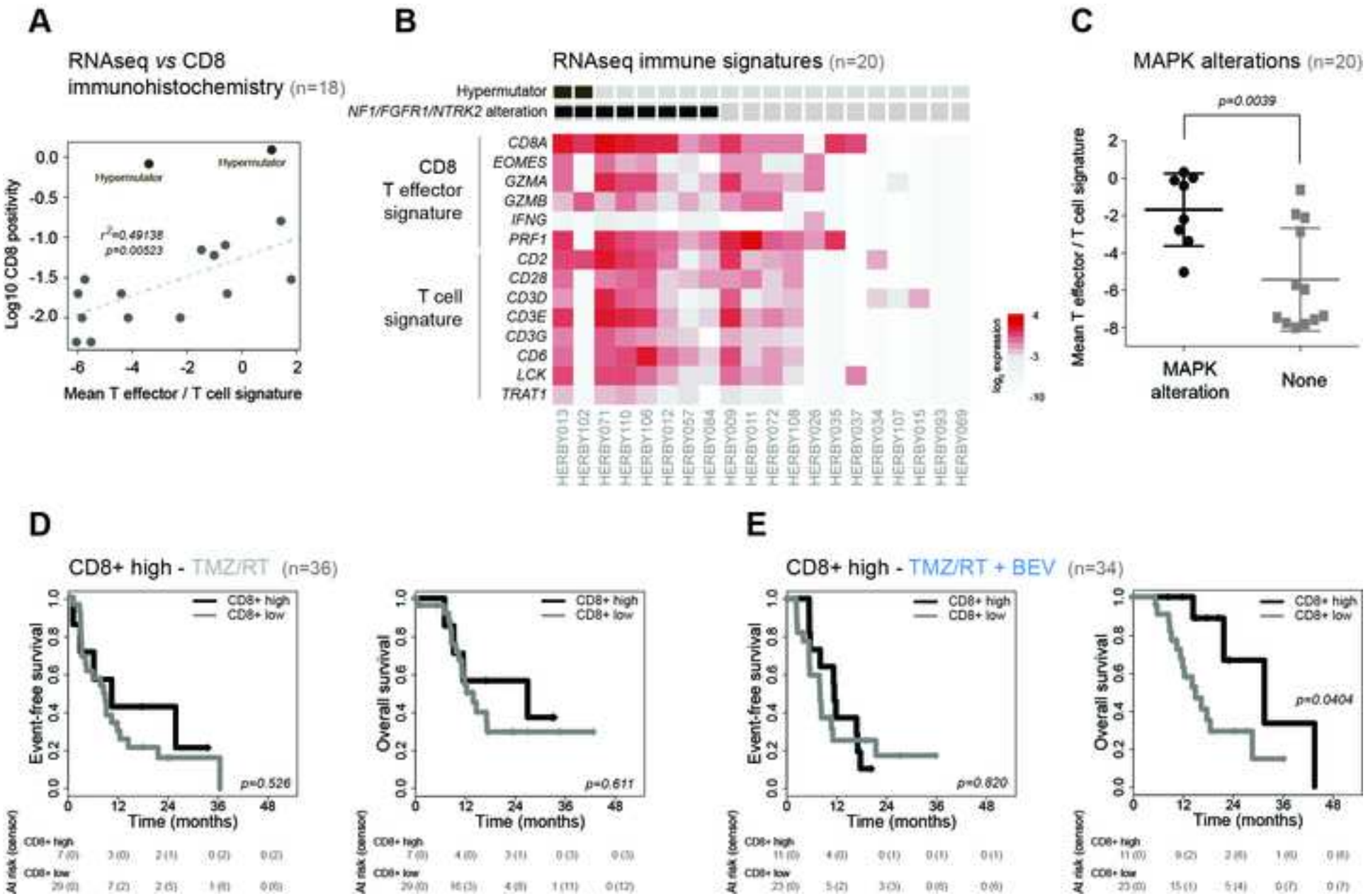

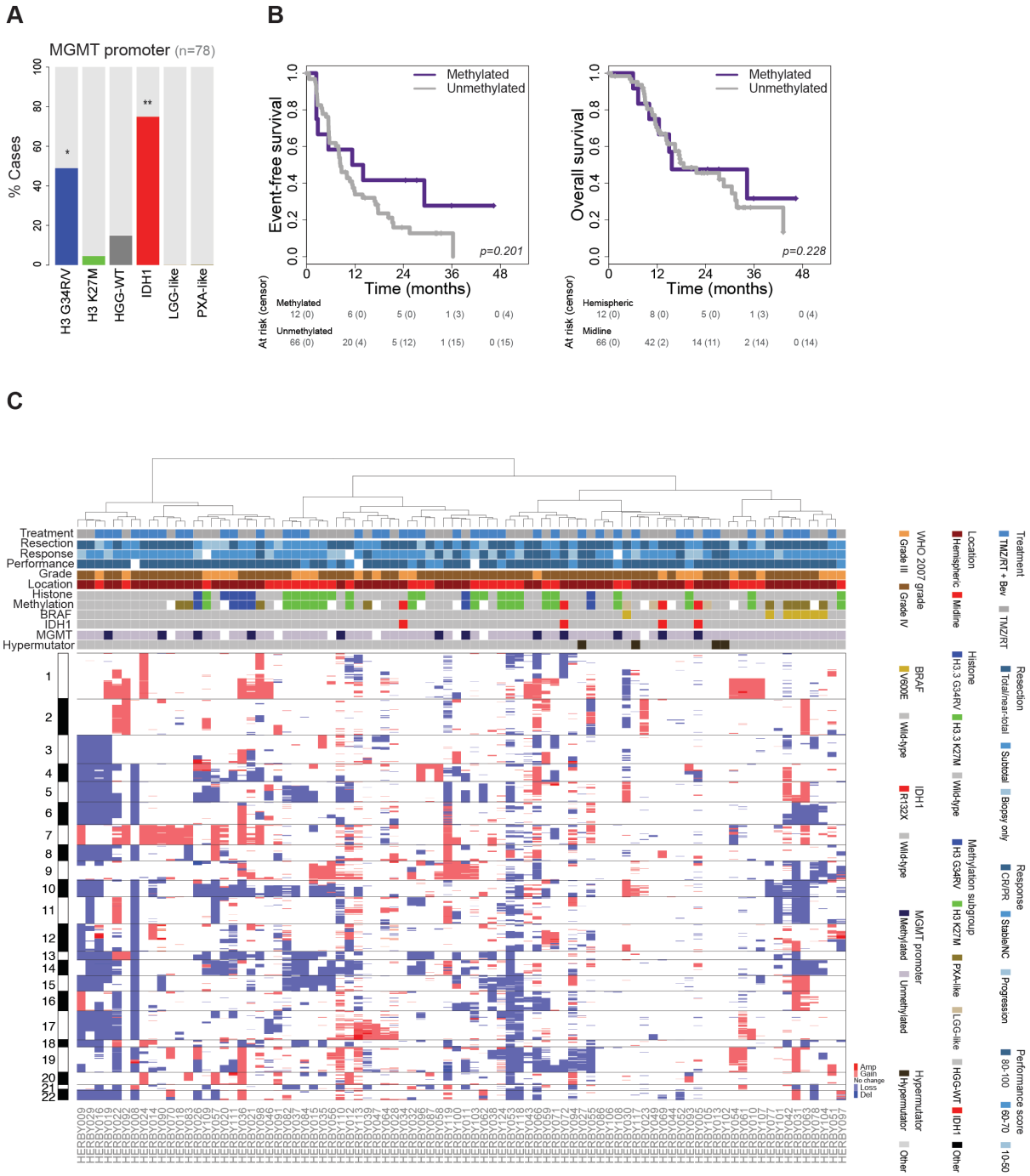

Figure S1 (related to Figure 2) – *MGMT promoter methylation.* (A) Barplots of number of cases with methylated *MGMT* promoter, subdivided by methylation subgroup. (B) Kaplan-Meier plot of event-free and overall survival of cases (y axis) separated by *MGMT* status, time given in months (x axis) and p value calculated by the log-rank test. (C) Heatmap representation of segmented DNA copy number for 86 samples derived from exome coverage data (dark red, amplification; red, gain; dark blue, deletion; blue, loss). Samples are arranged in columns clustered by gene-level data across the whole genome. Clinicopathological and molecular annotations are provided as bars according to the included key. CR/PR = complete response or partial response; Stable/NC = stable disease or no change.

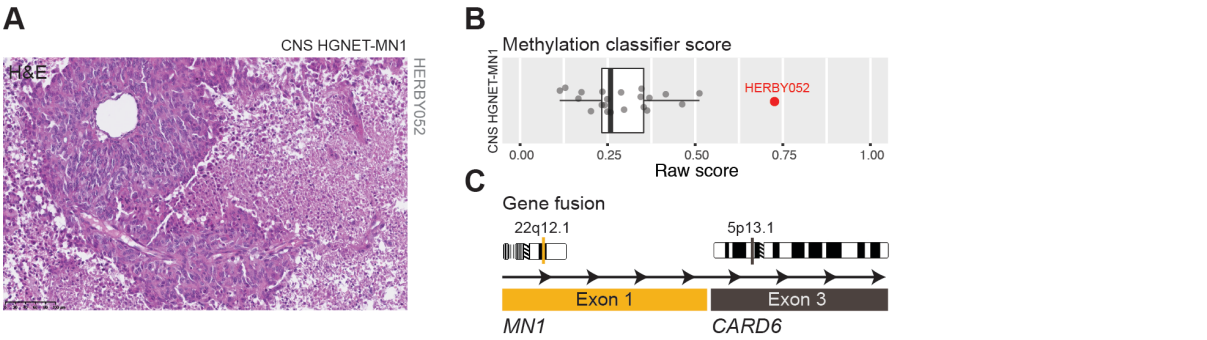
A
CNS HGNET-MN1
H&E
HERBY052
B
Methylation classifier score
CNS HGNET-MN1
HERBY052
0.00
0.25
0.50
0.75
1.00
Raw score
C
Gene fusion
22q12.1
5p13.1
Exon 1
Exon 3
MN1
CARD6

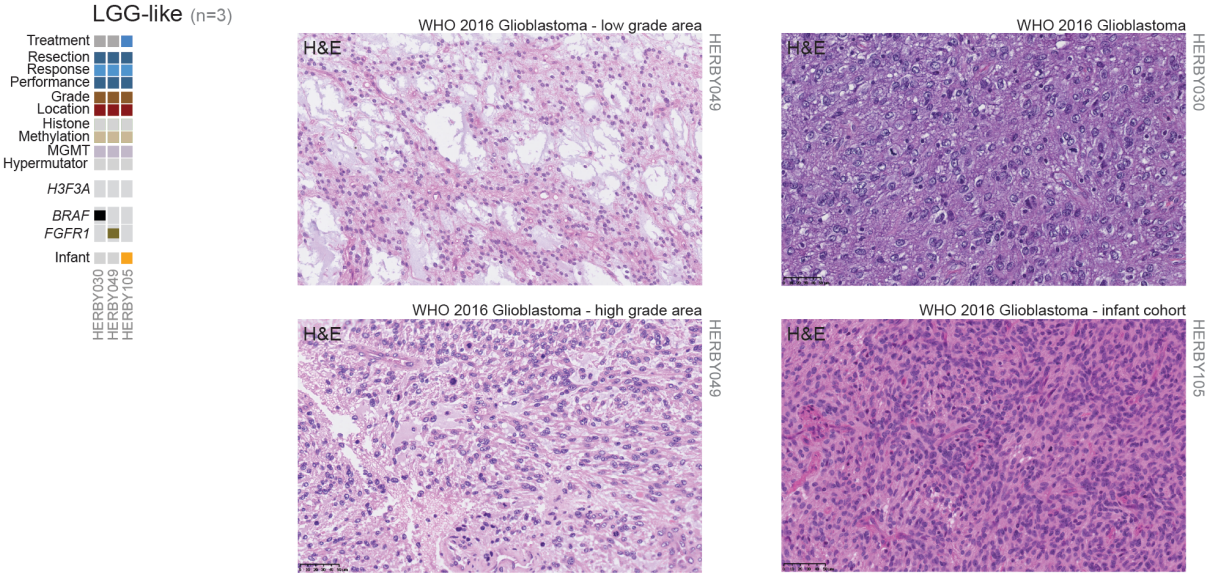
C
LGG-like (n=3)
Treatment
Resection
Response
Performance
Grade
Location
Histone
Methylation
MGMT
Hypermutator
H3F3A
BRAF
FGFR1
Infant
HERBY030
HERBY049
HERBY105
D
WHO 2016 Glioblastoma - low grade area
H&E
HERBY049
WHO 2016 Glioblastoma
H&E
HERBY030
WHO 2016 Glioblastoma - high grade area
H&E
HERBY049
WHO 2016 Glioblastoma - infant cohort
H&E
HERBY105

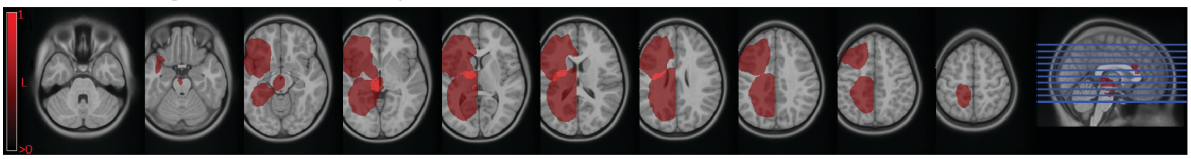
E
LGG-like radiological tumour lesion map
1
L
>0

Figure S2 (related to Figure 2) – *Alternate brain tumour entity and LGG-like cases*. (A) Haematoxylin and eosin staining of the case most closely resembling CNS HGNET-MN1, as demonstrated by a (B) boxplot of reference methylation classifier scores, and (C) the presence of a novel *MN1:CARD6* gene fusion by capture panel sequencing. (D) Integrated annotation of somatic mutations and DNA copy number changes in 9 samples classifying as LGG-like. (E) Haematoxylin and eosin staining of the three cases, all histologically classified as glioblastoma – (left) the presence of both low- and high grade areas of the tumour harbouring *BRAF*_V600E mutation; (top right) case harbouring an intragenic *FGFR1* duplication (both previous cases classifying as pilocytic astrocytoma); (bottom left) a cased from the infant cohort, with a methylation profile most closely resembling desmoplastic infantile ganglioglioma. (F) Radiological tumour lesion map of LGG-like cases. Brighter coloured pixels indicate a higher probability of tumour incidence.

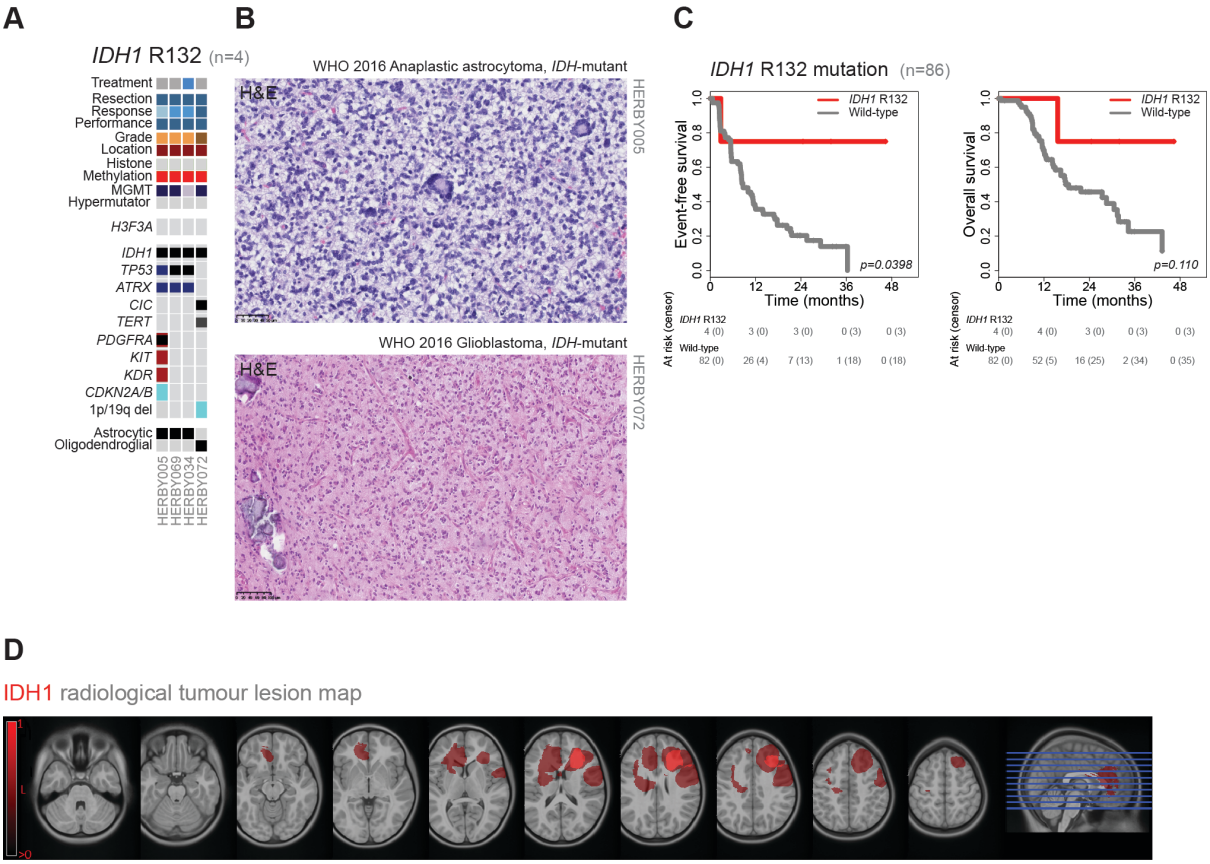

Figure S3 (related to Figure 2) – *IDH1 mutant tumours*. (A) Integrated annotation of somatic mutations and DNA copy number changes in 4 samples with *IDH1*_R132 mutation. (B) Haematoxylin and eosin staining of cases showing astrocytic (top) and oligodendroglial (bottom) histological features. (C) Kaplan-Meier plot of event-free and overall survival of cases (y axis) separated by *IDH1*_R132 status, time given in months (x axis) and p value calculated by the log-rank test. (D) Radiological tumour lesion map of IDH1 cases. Brighter coloured pixels indicate a higher probability of tumour incidence.

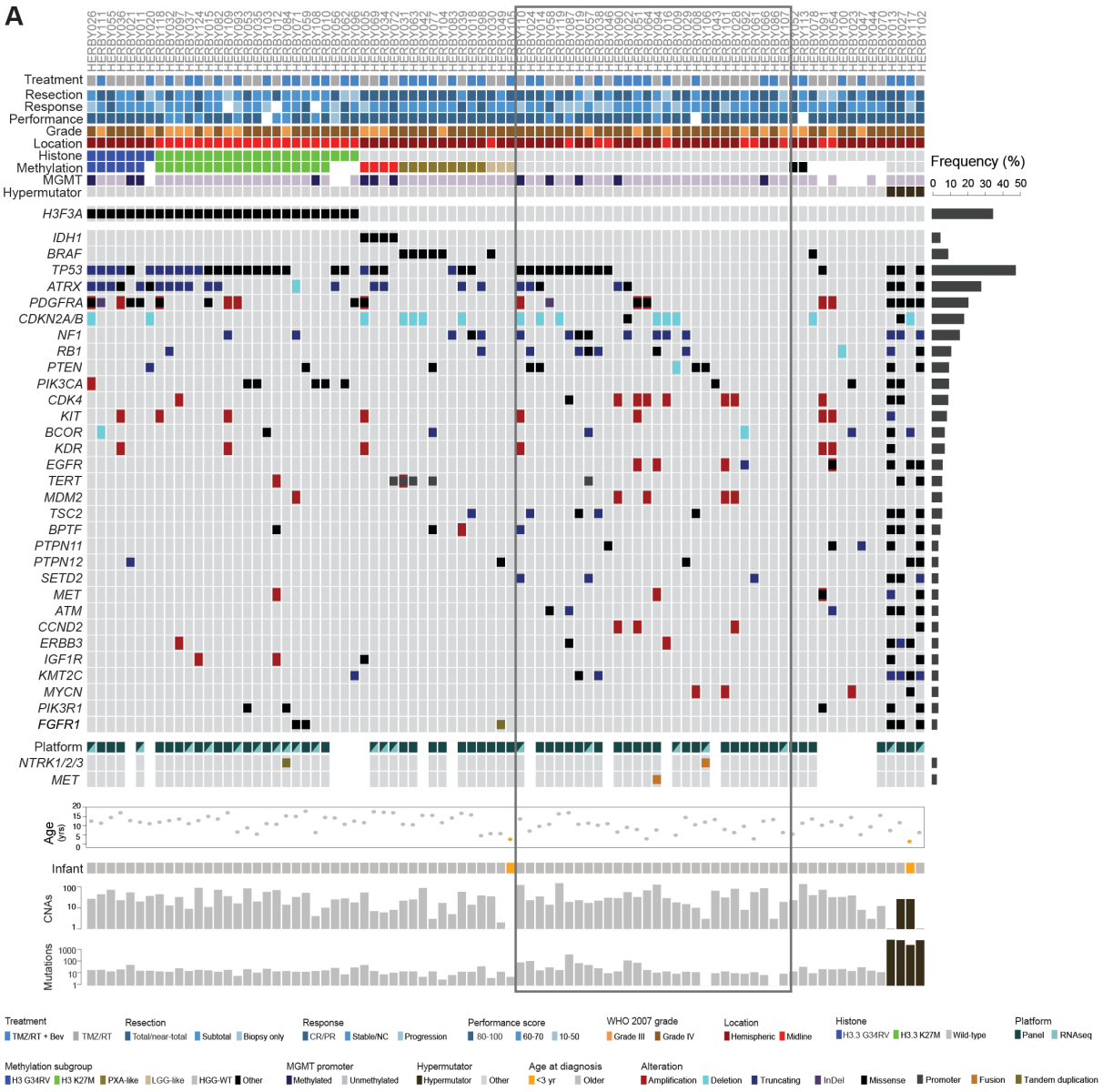

B

HGG-wt radiological tumour lesion map

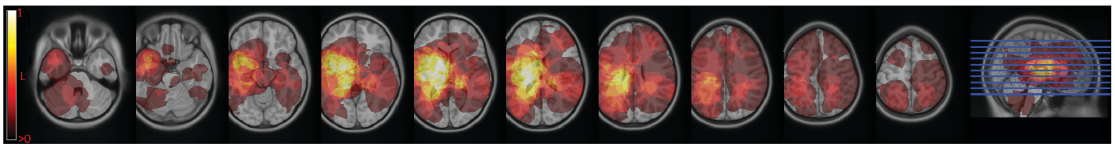

Figure S4 (related to Figure 3) – *Somatic mutations.* (A) Oncoprint representation of an integrated annotation of somatic mutations and DNA copy number changes for the 30 most frequently altered genes in 86 samples ($n \geq 3$, frequency barplot on the right, excluding hypermutator cases), ordered by histone and methylation subgroups. Selected common fusion events are also shown where available. Samples are arranged in columns with genes labelled along rows. Barplots are provided on a $\log_{10}$ scale for numbers of copy number aberrations and somatic mutations per case. Clinicopathological and molecular annotations are provided as bars according to the included key. CR/PR = complete response or partial response; Stable/NC = stable disease or no change. The annotated box highlights 'HGG-WT' tumours not otherwise assigned to a subgroup. (B) Radiological tumour lesion map of HGG-WT cases. Brighter coloured pixels indicate a higher probability of tumour incidence.

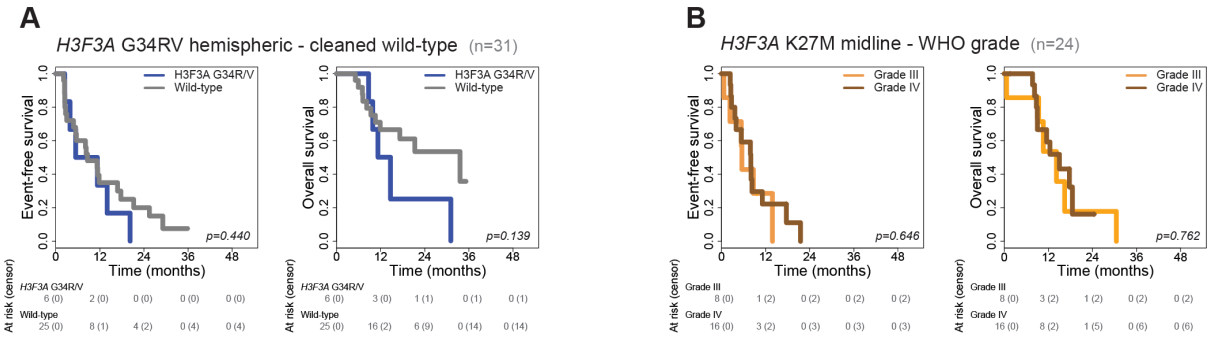

Figure S5 (related to Figure 4) – *H3F3A mutant subgroups*. (A) Kaplan-Meier plot of event-free and overall survival (y axis) of cerebral hemispheric cases, excluding those classified by methylation profiling as IDH1, PXA-like or LGG-like, separated by *H3F3A* status. Time is given in months (x axis) and p value calculated by the log-rank test. (B) Kaplan-Meier plot of event-free and overall survival (y axis) of midline *H3F3A*_K27M cases, separated by WHO grade. Time is given in months (x axis) and p value calculated by the log-rank test.

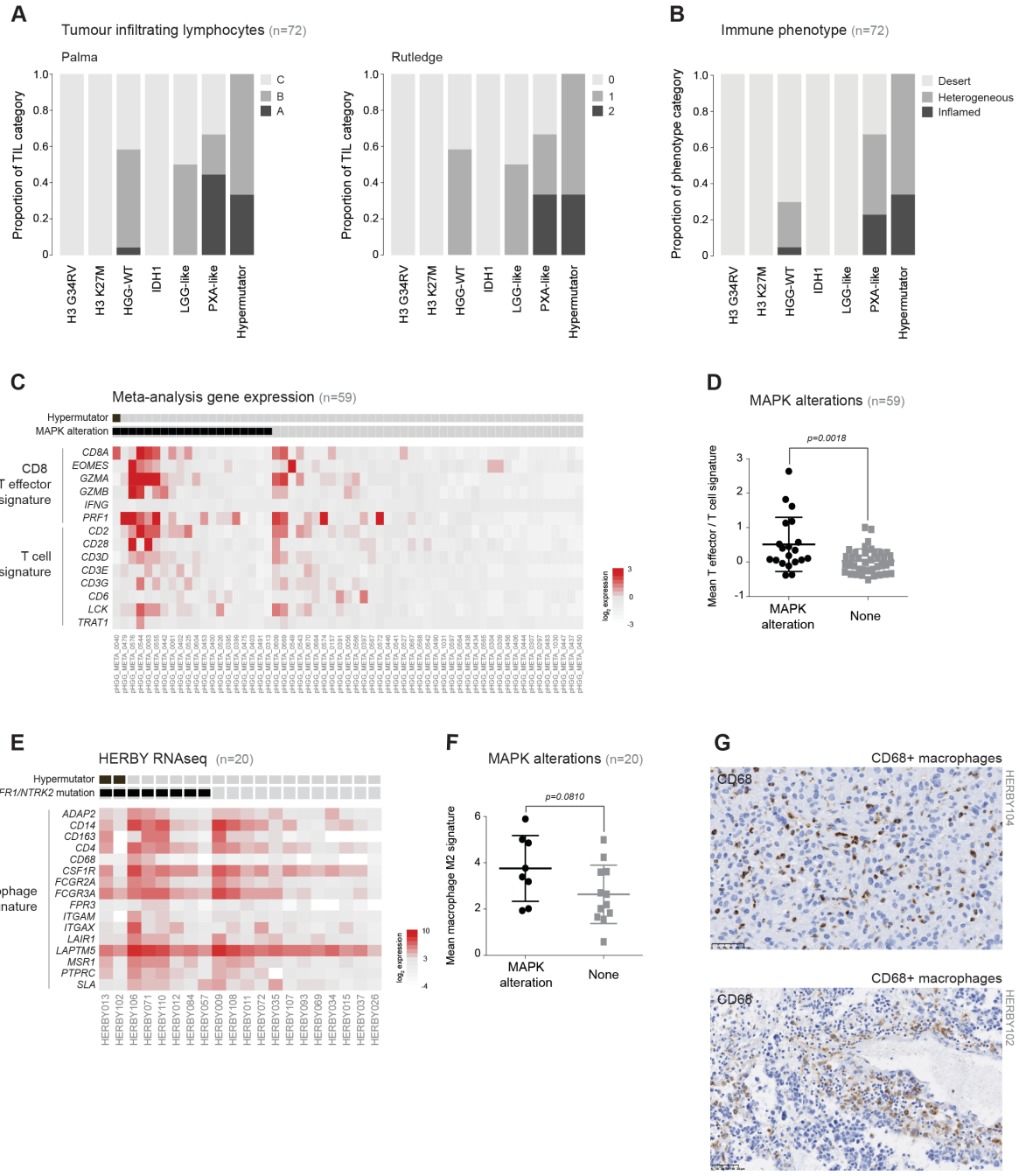
A
Tumour infiltrating lymphocytes (n=72)
Palma
Rutledge
Proportion of TIL category
C
B
A
0
1
2
H3 G34RV
H3 K27M
HGG-WT
IDH1
LGG-like
PXA-like
Hypermutator
B
Immune phenotype (n=72)
Proportion of phenotype category
Desert
Heterogeneous
Inflamed
C
Meta-analysis gene expression (n=59)
Hypermutator
MAPK alteration
CD8 T effector signature
CD8A
EOMES
GZMA
GZMB
IFNG
PRF1
T cell signature
CD2
CD28
CD3D
CD3E
CD3G
CD6
LCK
TRAT1
log2 expression
D
MAPK alterations (n=59)
p=0.0018
Mean T effector / T cell signature
MAPK alteration
None
E
HERBY RNAseq (n=20)
Hypermutator
NF1/FGFR1/NTRK2 mutation
Macrophage M2 signature
ADAP2
CD14
CD163
CD4
CD68
CSF1R
FCGR2A
FCGR3A
FPR3
ITGAM
ITGAX
LAIR1
LAPTM5
MSR1
PTPRC
SLA
log2 expression
F
MAPK alterations (n=20)
p=0.0810
Mean macrophage M2 signature
MAPK alteration
None
G
CD68+ macrophages
CD68
HERBY104
CD68+ macrophages
CD68
HERBY102

Figure S6 (related to Figure 7) – *Immune profiling*. (A) Barplot showing relative proportions of tumour-infiltrating lymphocytes categorised according to two schema (Palma and Rutledge), split by pHGG subgroups (B) Barplot showing relative proportions of histologically defined immune phenotype, split by pHGG subgroups. (C) Gene expression signatures for CD8 T effector and T cells plotted as a heatmap from combined gene expression data of non-brainstem high-grade glioma in n=58 patients aged 3-18 years from Mackay *et al.*, 2017. Hypermutator cases and those with MAPK alterations are annotated. (D) Boxplot of T effector / T cell gene expression values in MAPK altered samples compared to those without. Bold line represents the median, whiskers span the interquartile range. (E) Gene expression signatures for M2 macrophages plotted as a heatmap from RNAseq data. Hypermutator cases and those with MAPK alterations are annotated. (F) Boxplot of M2 macrophage cell gene expression values in MAPK altered samples compared to those without. Bold line represents the median, whiskers span the interquartile range. (G) Immunohistochemistry directed against CD68, showing positive cells in perivascular areas associated with lymphocytes (top, HERBY104, hypermutator) and more diffusely mixed with tumour cells (bottom, HERBY102, BRAF_V600E).

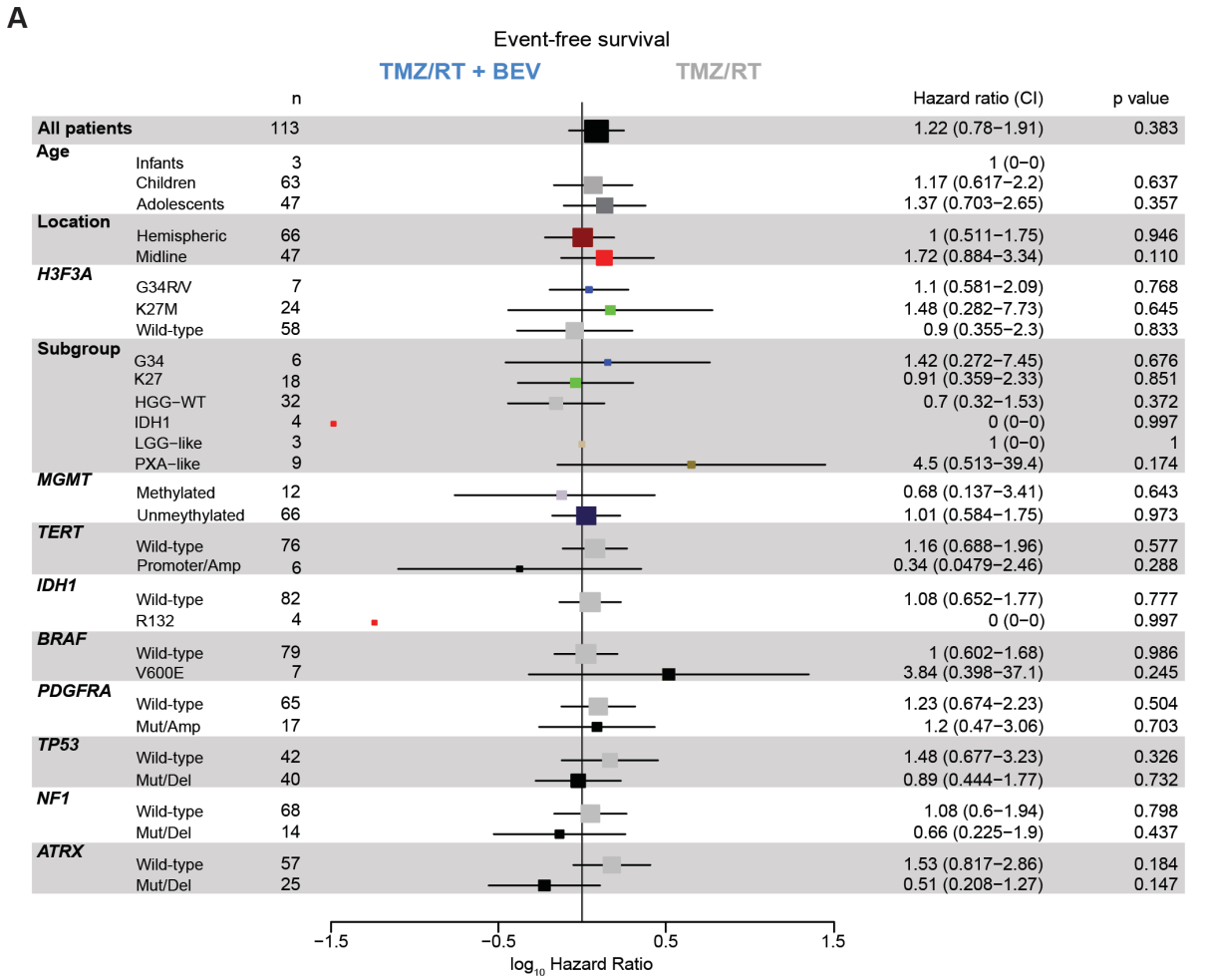
A
Event-free survival
TMZ/RT + BEV
TMZ/RT
n
Hazard ratio (CI)
p value
All patients 113 1.22 (0.78−1.91) 0.383
Age
Infants 3 1 (0−0)
Children 63 1.17 (0.617−2.2) 0.637
Adolescents 47 1.37 (0.703−2.65) 0.357
Location
Hemispheric 66 1 (0.511−1.75) 0.946
Midline 47 1.72 (0.884−3.34) 0.110
H3F3A
G34R/V 7 1.1 (0.581−2.09) 0.768
K27M 24 1.48 (0.282−7.73) 0.645
Wild-type 58 0.9 (0.355−2.3) 0.833
Subgroup
G34 6 1.42 (0.272−7.45) 0.676
K27 18 0.91 (0.359−2.33) 0.851
HGG−WT 32 0.7 (0.32−1.53) 0.372
IDH1 4 0 (0−0) 0.997
LGG−like 3 1 (0−0) 1
PXA−like 9 4.5 (0.513−39.4) 0.174
MGMT
Methylated 12 0.68 (0.137−3.41) 0.643
Unmeythylated 66 1.01 (0.584−1.75) 0.973
TERT
Wild-type 76 1.16 (0.688−1.96) 0.577
Promoter/Amp 6 0.34 (0.0479−2.46) 0.288
IDH1
Wild-type 82 1.08 (0.652−1.77) 0.777
R132 4 0 (0−0) 0.997
BRAF
Wild-type 79 1 (0.602−1.68) 0.986
V600E 7 3.84 (0.398−37.1) 0.245
PDGFRA
Wild-type 65 1.23 (0.674−2.23) 0.504
Mut/Amp 17 1.2 (0.47−3.06) 0.703
TP53
Wild-type 42 1.48 (0.677−3.23) 0.326
Mut/Del 40 0.89 (0.444−1.77) 0.732
NF1
Wild-type 68 1.08 (0.6−1.94) 0.798
Mut/Del 14 0.66 (0.225−1.9) 0.437
ATRX
Wild-type 57 1.53 (0.817−2.86) 0.184
Mut/Del 25 0.51 (0.208−1.27) 0.147
−1.5
−0.5
0.5
1.5
log10 Hazard Ratio

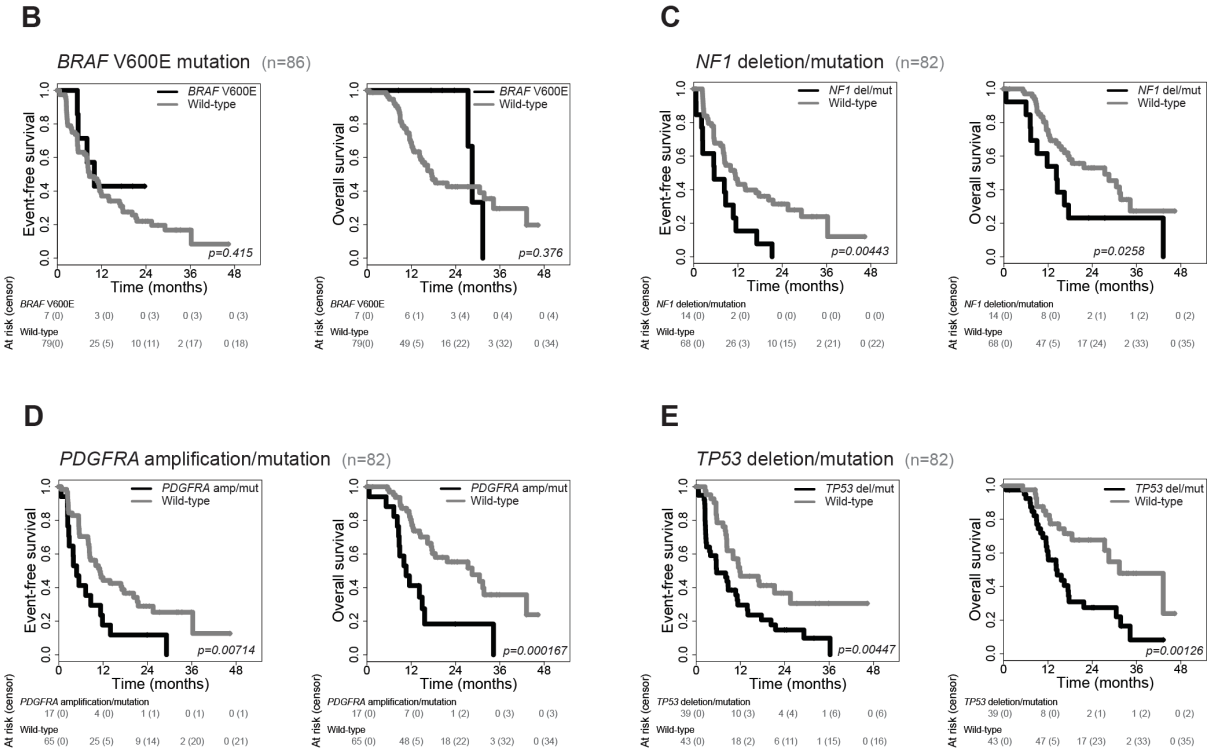
B
BRAF V600E mutation (n=86)
Event-free survival
Overall survival
BRAF V600E
Wild-type
p=0.415
p=0.376
Time (months)
At risk (censor)
BRAF V600E 7 (0) 3 (0) 0 (3) 0 (3) 0 (3)
Wild-type 79 (0) 25 (5) 10 (11) 2 (17) 0 (18)
BRAF V600E 7 (0) 6 (1) 3 (4) 0 (4) 0 (4)
Wild-type 79 (0) 49 (5) 16 (22) 3 (32) 0 (34)
C
NF1 deletion/mutation (n=82)
NF1 del/mut
Wild-type
p=0.00443
p=0.0258
NF1 deletion/mutation 14 (0) 2 (0) 0 (0) 0 (0) 0 (0)
Wild-type 68 (0) 26 (3) 10 (15) 2 (21) 0 (22)
NF1 deletion/mutation 14 (0) 8 (0) 2 (1) 1 (2) 0 (2)
Wild-type 68 (0) 47 (5) 17 (24) 2 (33) 0 (35)
D
PDGFRA amplification/mutation (n=82)
PDGFRA amp/mut
Wild-type
p=0.00714
p=0.000167
PDGFRA amplification/mutation 17 (0) 4 (0) 1 (1) 0 (1) 0 (1)
Wild-type 65 (0) 25 (5) 9 (14) 2 (20) 0 (21)
PDGFRA amplification/mutation 17 (0) 7 (0) 1 (2) 0 (3) 0 (3)
Wild-type 65 (0) 48 (5) 18 (22) 3 (32) 0 (34)
E
TP53 deletion/mutation (n=82)
TP53 del/mut
Wild-type
p=0.00447
p=0.00126
TP53 deletion/mutation 39 (0) 10 (3) 4 (4) 1 (6) 0 (6)
Wild-type 43 (0) 18 (2) 6 (11) 1 (15) 0 (16)
TP53 deletion/mutation 39 (0) 8 (0) 2 (1) 1 (2) 0 (2)
Wild-type 43 (0) 47 (5) 17 (23) 2 (33) 0 (35)

Figure S7 (related to Figure 7) – *Exploratory biomarker analysis*. (A) Hazard ratio plot for a univariate Cox regression analysis on a variety of molecular subgroups and alterations in respect of event-free survival. Log_2 hazard ratios less than zero indicate a better response to TMZ/RT plus BEV, ratios greater than zero a better response to TMZ/RT alone. Median (box) and 95% confidence intervals (whiskers) are plotted, with size of box proportion to sample size on an indicated category of tumours. Kaplan-Meier plot of event-free and overall survival of cases (y axis) separated by (B) *BRAF* V600E, (C) *NF1*, (D) *PDGFRA* and (E) *TP53* status, time given in months (x axis) and p value calculated by the log-rank test.

Supplementary Table S1

Supplementary Table S2

Click here to access/download

Supplemental Videos and Spreadsheets

HERBY.biology.Supplementary.Table.S2.Feb18.xlsx